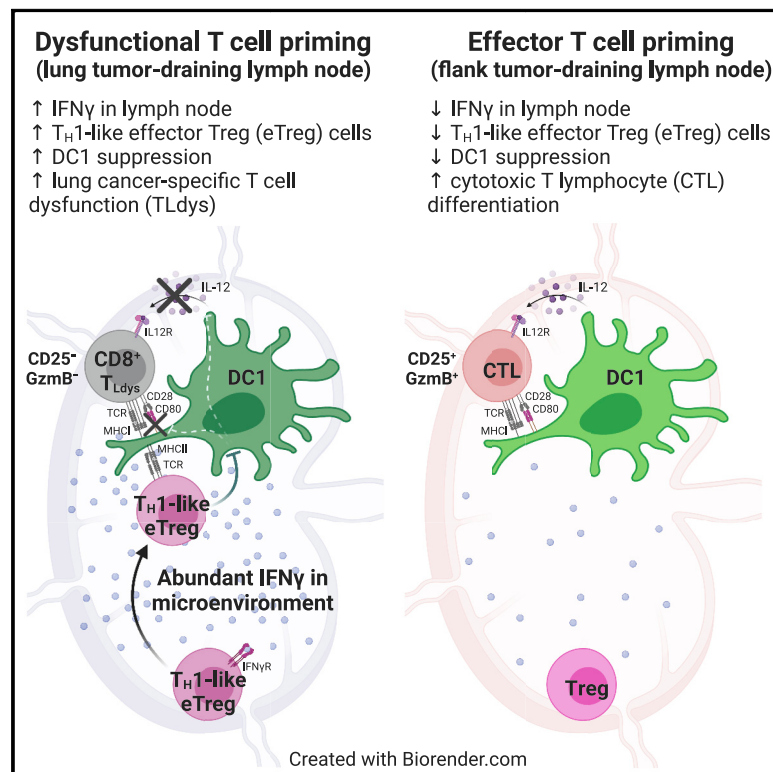


Immunity

Tissue-specific abundance of interferon-gamma drives regulatory T cells to restrain DC1-mediated priming of cytotoxic T cells against lung cancer

Graphical abstract



Authors

Maria Zagorulya, Leon Yim,
Duncan M. Morgan, ..., K. Dane Wittrup,
J. Christopher Love, Stefani Spranger

Correspondence

spranger@mit.edu

In brief

How tissue-specific mechanisms shape anti-tumor immunity remains poorly understood. Zagorulya et al. reveal that lung lymph node (LN)-specific abundance of interferon-gamma induces suppressive Th1-like effector regulatory T (Treg) cells. These effector Treg cells interact with type 1 conventional dendritic cells and restrain priming of cytotoxic T cell responses against lung cancer.

Highlights

- Lung LN-specific enrichment in IFN- γ induces suppressive Th1-like effector Treg cells
- LN microniches skew Treg cells to be Th1-like and drive DC1 suppression
- Suppressed DC1s prime dysfunctional CD8⁺ T cell responses against lung cancer
- IFN- γ blockade repolarizes Treg cells and restores CTL priming against lung cancer



Article

Tissue-specific abundance of interferon-gamma drives regulatory T cells to restrain DC1-mediated priming of cytotoxic T cells against lung cancer

Maria Zagorulya,^{1,2} Leon Yim,¹ Duncan M. Morgan,^{1,3} Austin Edwards,⁴ Elen Torres-Mejia,¹ Noor Momin,^{1,5} Chloe V. McCreery,^{1,5} Izabella L. Zamora,^{1,6} Brendan L. Horton,¹ James G. Fox,^{5,7} K. Dane Wittrup,^{1,3,5} J. Christopher Love,^{1,3,8} and Stefani Spranger^{1,2,8,9,*}

¹Koch Institute for Integrative Cancer Research, MIT, Cambridge, MA 02139, USA

²Department of Biology, MIT, Cambridge, MA 02139, USA

³Department of Chemical Engineering, MIT, Cambridge, MA 02139, USA

⁴Biological Imaging Development CoLab, UCSF, San Francisco, CA 94143, USA

⁵Department of Biological Engineering, MIT, Cambridge, MA 02139, USA

⁶Department of Electrical Engineering and Computer Science, MIT, Cambridge, MA 02139, USA

⁷Division of Comparative Medicine, MIT, Cambridge, MA 02139, USA

⁸Ragon Institute of MGH, MIT and Harvard, Cambridge, MA 02139, USA

⁹Lead contact

*Correspondence: spranger@mit.edu

<https://doi.org/10.1016/j.immuni.2023.01.010>

SUMMARY

Local environmental factors influence CD8⁺ T cell priming in lymph nodes (LNs). Here, we sought to understand how factors unique to the tumor-draining mediastinal LN (mLN) impact CD8⁺ T cell responses toward lung cancer. Type 1 conventional dendritic cells (DC1s) showed a mLN-specific failure to induce robust cytotoxic T cells responses. Using regulatory T (Treg) cell depletion strategies, we found that Treg cells suppressed DC1s in a spatially coordinated manner within tissue-specific microniches within the mLN. Treg cell suppression required MHC II-dependent contact between DC1s and Treg cells. Elevated levels of IFN- γ drove differentiation Treg cells into Th1-like effector Treg cells in the mLN. In patients with cancer, Treg cell Th1 polarization, but not CD8⁺/Treg cell ratios, correlated with poor responses to checkpoint blockade immunotherapy. Thus, IFN- γ in the mLN skews Treg cells to be Th1-like effector Treg cells, driving their close interaction with DC1s and subsequent suppression of cytotoxic T cell responses.

INTRODUCTION

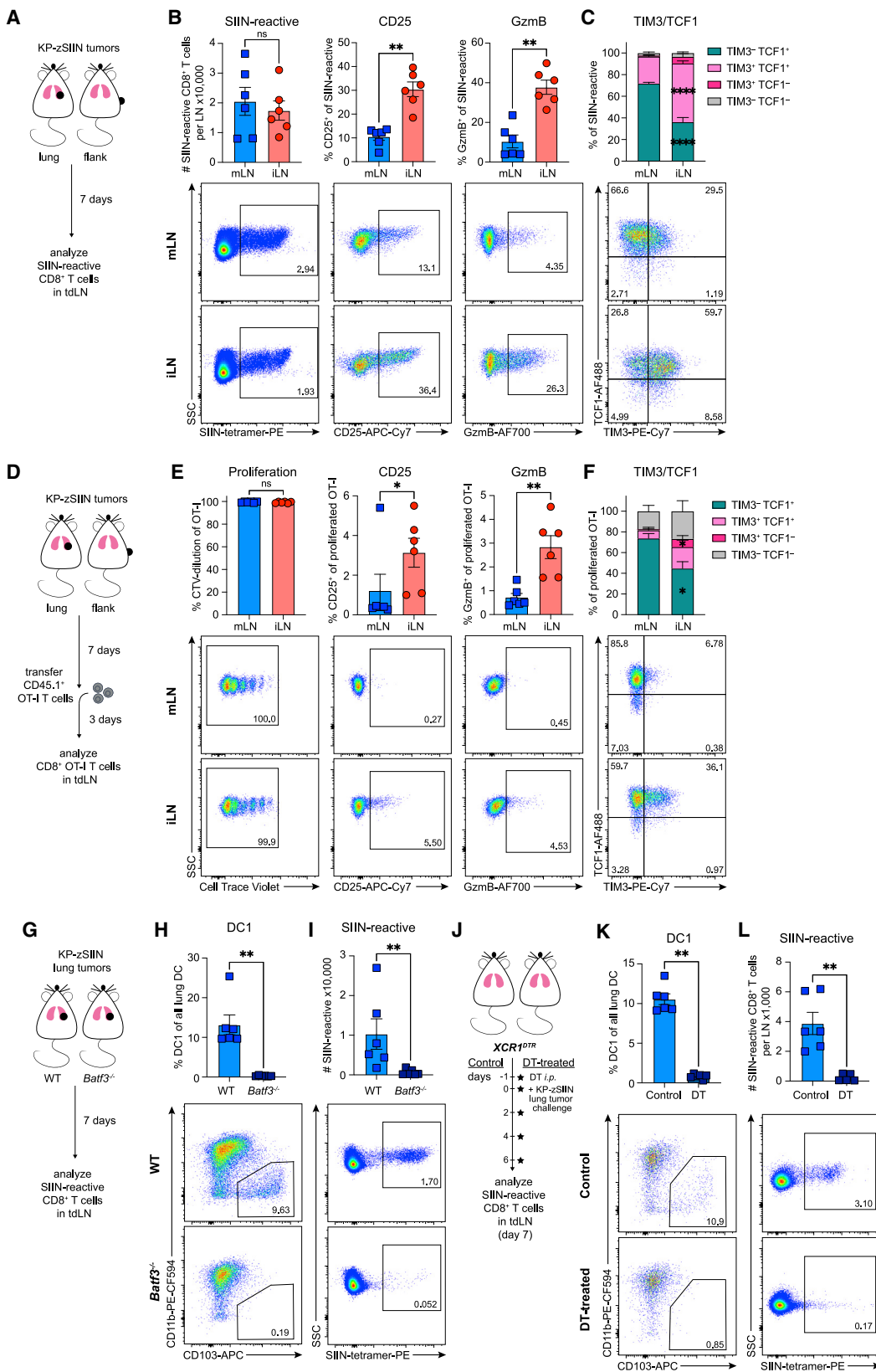
Cytotoxic CD8⁺ T cells are essential for anti-tumor immunity.^{1,2} Naive CD8⁺ T cells acquire cytotoxic function following priming by type 1 conventional dendritic cells (DC1s) in the tumor-draining lymph nodes (tdLNs).^{3–5} DC1s prime naive T cells by providing three distinct stimulatory signals.⁶ Signal 1 is cognate antigen, cross-presented on the major histocompatibility complex class I (MHC-I) on DC1s.^{4,5,7,8} Signal 2 comprises costimulatory ligands, such as CD80 and CD86, expressed on activated DC1s,^{9–13} and signal 3 refers to cytokines, including DC-derived interleukin-12 (IL-12), that promote differentiation into cytotoxic T lymphocytes (CTLs).^{14–17} The functional capacity of activated CD8⁺ T cells depends on the abundance, timing, and context of these signals on DC1s.^{18–22}

Distinct T cell activation trajectories established early after priming can have long-term effects on the quality of CD8⁺ T cell responses. For instance, elevated TOX expression four days post-chronic viral infection mediates commitment to the T cell exhaustion program.²³ In lung cancer, priming induces a

T cell dysfunction program that prevents CTL differentiation and drives resistance to immune checkpoint blockade (ICB) therapy.²⁴ Hence, DC1-derived signals available during priming are instrumental for shaping the quality of the anti-tumor T cell response.²⁵

The local environment regulates DC capacity to prime T cell responses.²⁵ At baseline, DCs have low expression of signals 2 and 3 and are poorly stimulatory.^{26–29} In the absence of signals 2 and 3, cognate antigen-presenting DCs induce T cell tolerance, characterized by initial proliferation with failed accumulation and eventual T cell deletion.^{30–32} Exposure to danger signals, such as tumor-derived double-stranded DNA (dsDNA), promotes DC maturation and expression of signal 2 and 3 molecules.^{27–29} DC stimulatory capacity can be regulated by other immune cells, most notably by regulatory T (Treg) cells. Treg cells inhibit DC maturation and cause decreased expression of signals 2 and 3.^{33–39} Treg cell-mediated suppression of DC stimulatory capacity in tumors can blunt protective anti-tumor CD8⁺ T cell responses.^{38,40,41} Additionally, tissue-specific factors and microanatomical niches in the draining LNs influence DC ability





(legend on next page)

to prime distinct T cell subsets.⁴² For instance, DCs in lung and gut LNs can imprint tissue-specific homing receptor expression on T cells.^{43–45} Moreover, DCs can skew T cell responses toward effector, tolerance, or memory programs in a tissue-specific manner.^{46,47} Within a draining LN, the microanatomical location of DC1s and CD8⁺ T cells during priming dictates T cell exposure to stimulatory signals and influences effector differentiation.^{48,49} Thus, several environmental factors can impact the T cell activation program induced during priming.

How tissue-specific immunoregulatory mechanisms influence anti-tumor T cell responses remains poorly understood. In this study, we sought to uncover lung cancer-specific mechanisms driving dysfunctional tumor-reactive CD8⁺ T cells during T cell priming.²⁴ By comparing T cell responses in the mediastinal (mLN) and inguinal (iLN) LN that drained lung and flank tumors, respectively, we determined that Treg cells in the mLN restrained DC1-mediated priming of CTLs more effectively than their counterparts in the iLN. Treg cell-driven suppression of DC1s caused dysfunctional CD8⁺ T cell responses against lung tumors and required MHC-II-dependent contact between Treg cells and DC1s. Suppressive, clonally expanded T helper 1 (Th1)-like Treg cells were preferentially induced in the mLN in response to the tissue-specific abundance of interferon-gamma (IFN- γ). Blockade of IFN- γ was sufficient to repolarize Treg cells and rescue CTL responses against lung tumors. Thus, tissue-specific induction of Th1-like Treg cells that suppress DC1-mediated CTL priming could represent a critical barrier to anti-tumor immunity.

RESULTS

DC1s in mLNs prime dysfunctional CD8⁺ T cells against lung KP tumors

To study how priming of CTLs is restrained in lung cancer,²⁴ we compared T cell responses against tumors growing orthotopically in the lungs or subcutaneously in the flanks. We used the *Kras*^{G12D} *Trp53*^{−/−} (KP) lung adenocarcinoma cell line, engineered to express the model antigen SIINFEKL fused to ZsGreen (ZsG) (KP-zSIIN).^{24,50} We examined activation of SIIN-reactive CD8⁺ T cells in the mLN and iLN 7 days post-tumor implantation (Figure 1A). Despite comparable accumulation in both LNs, SIIN-reactive T cells primed in the mLN failed to express effector differentiation markers CD25 and granzyme B (GzmB) (Figure 1B), consistent with prior work.²⁴ This dysfunctional phenotype contrasted with the robust expression of effector

molecules on SIIN-reactive T cells primed in the iLN (Figure 1B). Induction of CTLs in the iLN was underscored by the increased expression of T cell immunoglobulin and mucin domain-containing protein 3 (TIM3) relative to the mLN (Figure 1C).

We validated that the observed phenotypic and functional differences²⁴ were independent of T cell receptor (TCR) signal strength using an *in vivo* priming assay. SIIN-reactive OT-I T cells activated in the mLN exhibited robust proliferation yet reduced expression of CD25, GzmB, and TIM3 (Figures 1D–1F, S1A, and S1B). We affirmed that the dysfunction phenotype was not specific to the SIIN antigen using KP-SIY (SIYRYYGL) cells²⁴ (Figures S1C–S1E).

Given the importance of cross-presenting DC1s for mounting anti-tumor immune responses,^{4,51} we next tested whether DC1s were the dominant DC subset priming tumor-reactive T cells in both LNs. SIIN-reactive T cell activation against both lung and flank tumors was severely impaired in *Batf3*^{−/−} mice lacking DC1s⁴ (Figures 1G–1I, S1F–S1K). We further validated the requirement of DC1s for priming tumor-reactive T cells in the mLN using the *XCR1*^{DTR} mouse model⁵² (Figures 1J–1L) and KP-SIY tumor cells (Figures S1L and S1M). Because DC2s can also prime productive anti-tumor CD8⁺ T cell responses,⁵³ we compared the functional capacity of DC1s and DC2s for activating CD8⁺ T cells. Using ZsG fluorescence as a readout for tumor antigen uptake, we isolated ZsG⁺ and ZsG[−] DC1s and DC2s from both tdLNs for *ex vivo* co-cultures (Figure S1N). ZsG⁺ DCs, but not ZsG[−] DCs, induced robust T cell proliferation, confirming that tumor-associated antigen was restricted to the ZsG⁺ fraction (Figures S1O and S1P). While both ZsG⁺ DC subsets could activate T cells, only ZsG⁺ DC1s induced productive priming, resulting in enhanced T cell proliferation and accumulation (Figures S1O and S1P). These data indicate that DC1s were the main DC subset activating tumor-reactive CD8⁺ T cells in both tdLNs.

DC1s in tumor-draining mLNs have high signal 1 but low signals 2 and 3

DCs exist in distinct functional states with varied expression of signals 1 (antigen), 2 (costimulation), and 3 (cytokines), which shape the quality of anti-tumor immunity.^{53,54} Because DC1s primed phenotypically distinct CD8⁺ T cell responses in the tumor-draining mLN and iLN (Figures 1A–L and S1A–S1M), we hypothesized that tissue-specific differences in DC1 states mediated the distinct priming outcomes. Therefore, we

Figure 1. DC1s in mLNs prime dysfunctional CD8⁺ T cells against lung KP tumors

- (A) Experimental design for (B–C).
- (B–C) Representative flow plots and (B) numbers of CD25, GzmB, (C) TCF1, and TIM-3 expression of SIIN-reactive CD8⁺ T cells in tdLNs, day 7 post-tumor implantation ($n = 3$ mice/group; two independent experiments).
- (D) Experimental design for (E–F).
- (E–F) Representative flow plots and quantified (E) CellTrace Violet (CTV) dilution or CD25, GzmB, (F) TCF1, and TIM-3 expression of adoptively transferred CTV-labelled OT-I T cells primed in tdLNs, day 10 post-tumor implantation ($n = 3$ mice/group; two independent experiments).
- (G) Experimental design for (H–I).
- (H–I) Representative flow plots and quantified abundance of (H) DC1s in lungs and (I) SIIN-reactive CD8⁺ T cells in mLNs of tumor-bearing WT or *Batf3*^{−/−} mice, day 7 post-tumor implantation ($n = 3$ mice/group; two independent experiments).
- (J) Experimental design for (K–L).
- (K–L) Representative flow plots and quantified abundance of (K) DC1s in lungs and (L) SIIN-reactive CD8⁺ T cells in mLNs of control or DT-treated tumor-bearing *XCR1*^{DTR} mice, day 7 post-tumor implantation ($n = 3$ mice/group; two independent experiments).

* $p < 0.05$, ** $p < 0.01$, *** $p < 0.0001$, ns = not significant; Mann-Whitney U test (MWU) (B–C, E–F, H–I, K–L). Data shown as mean \pm SEM.

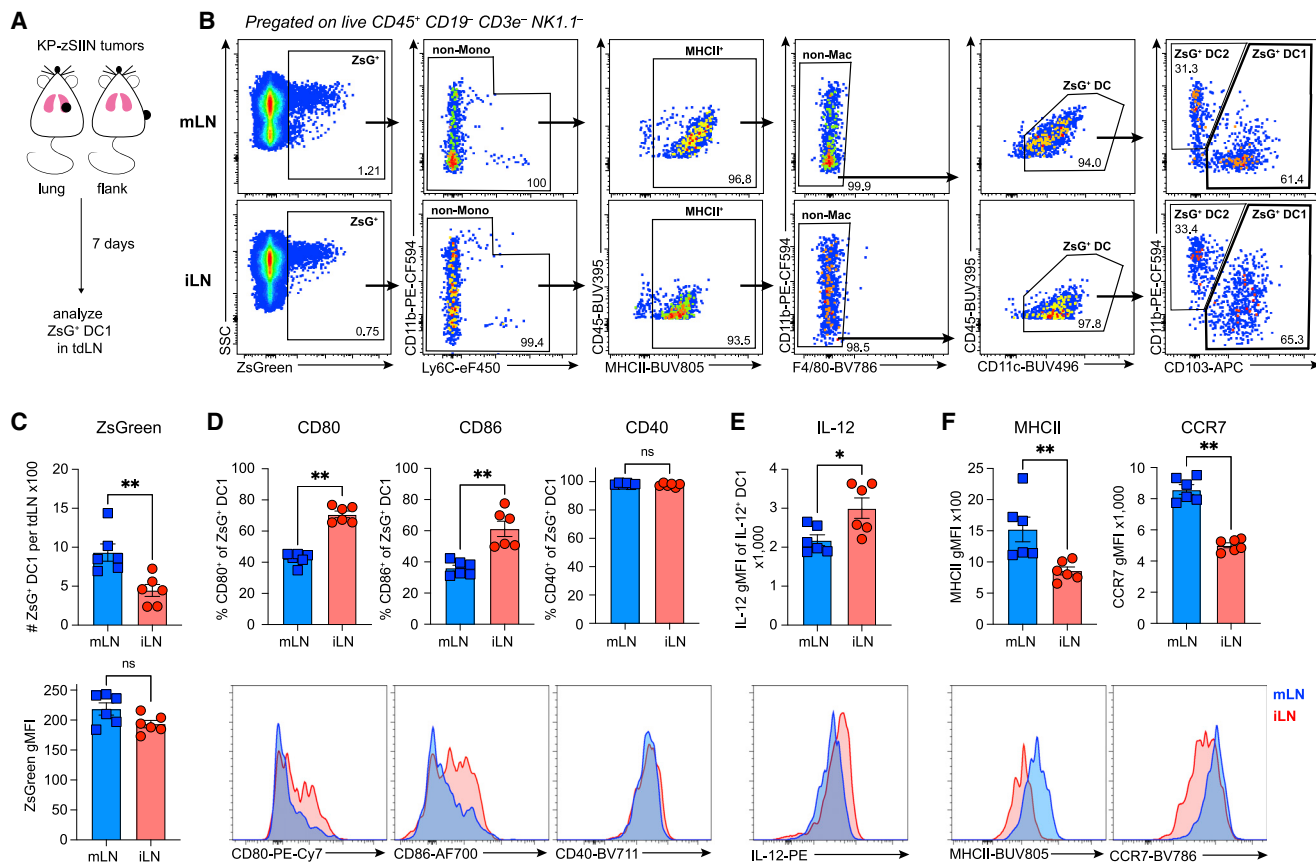


Figure 2. DC1s in tumor-draining mLN have high signal 1 but low signals 2 and 3

(A) Experimental design for (B)–(F).

(B) Representative flow gating strategy for ZsG⁺ DC1s from tdLN.

(C) (Top) Abundance and (bottom) ZsG geometric mean fluorescence intensity (gMFI) of ZsG⁺ DC1s from tdLN, day 7 post-tumor implantation (LNs from 3 to 4 mice pooled per datapoint; two independent experiments).

(D–F) Representative histograms and quantified expression of (D) CD80, CD86, CD40, (E) IL-12, (F) MHC-II, and CCR7 on ZsG⁺ DC1s from tdLN, day 7 post-tumor implantation (LNs from 3 to 4 mice pooled per datapoint; two independent experiments).

*p < 0.05, **p < 0.01, ns = not significant; MWU (C)–(F). Data shown as mean ± SEMs.

characterized signals 1, 2, and 3 on tumor-derived ZsG⁺ DC1s in both tdLN (Figures 2A and 2B).

ZsG⁺ DC1 abundance was increased in the mLN compared with the iLN, with similar ZsG intensity, suggesting no defect in DC1 ability to engulf tumor debris and migrate to the tumor-draining mLN (Figure 2C). ZsG⁺ DC1s from both LNs also had equal ability to prime naive CD8⁺ T cells ex vivo (Figures S1N–S1P), underscoring that DC1s from the mLN were not deficient in signal 1. Expression of CD80 and CD86 was reduced, while CD40 was unchanged on ZsG⁺ DC1s from mLN compared with those in the iLN (Figure 2D). Further, ZsG⁺ DC1s from the mLN produced less IL-12 relative to their counterparts in the iLN (Figure 2E). Because low expression of signals 2 (CD80 and CD86) and 3 (IL-12) is characteristic of immature DCs,^{55,56} we examined the maturation markers MHC-II and CCR7. Both molecules were highly expressed on ZsG⁺ DC1s from the mLN (Figure 2F). We concluded that tumor-derived DC1s in the mLN were highly mature and provided sufficient signal 1 yet had reduced expression of CD80, CD86, and IL-12, required for priming of true CTLs.

Because mature DCs can acquire immunoregulatory molecules (mregDCs) and suppress anti-tumor immunity following engulfment of tumor debris,⁵⁴ we examined mregDC markers (CD40, IL-12, and PD-L1).⁵⁴ We observed similar expression of CD40 (Figure 2D) while IL-12 and PD-L1 were reduced on ZsG⁺ DC1s from mLN relative to iLN (Figures 2E, S1Q, and S1R). Further, the mLN-specific decrease in CD80, CD86, and IL-12 expression (Figures 2D and 2E) was also detected on ZsG⁺ DC1s (Figures S1S–S1U), suggesting a tissue-specific suppression distinct from the mregDC program.

Reduced expression of CD80, CD86, and IL-12 on DC1s from the tumor-draining mLN (Figures 2D, 2E, and S1S–S1U) could indicate DC1-intrinsic tissue-specific suppression. However, the tissue-specific differences in signal 2 and 3 on DC1s (Figures 2D, 2E, and S1S–S1U) were no longer detectable in naive mice (Figures S1V–S1X), suggesting that the suppressed phenotype was not an intrinsic property of DC1s in the mLN. Additionally, compared with the mLN-specific induction of dysfunctional CD8⁺ T cells *in vivo* (Figures 1D and 1E), ZsG⁺ DC1s from both LNs primed CTLs with a similarly high

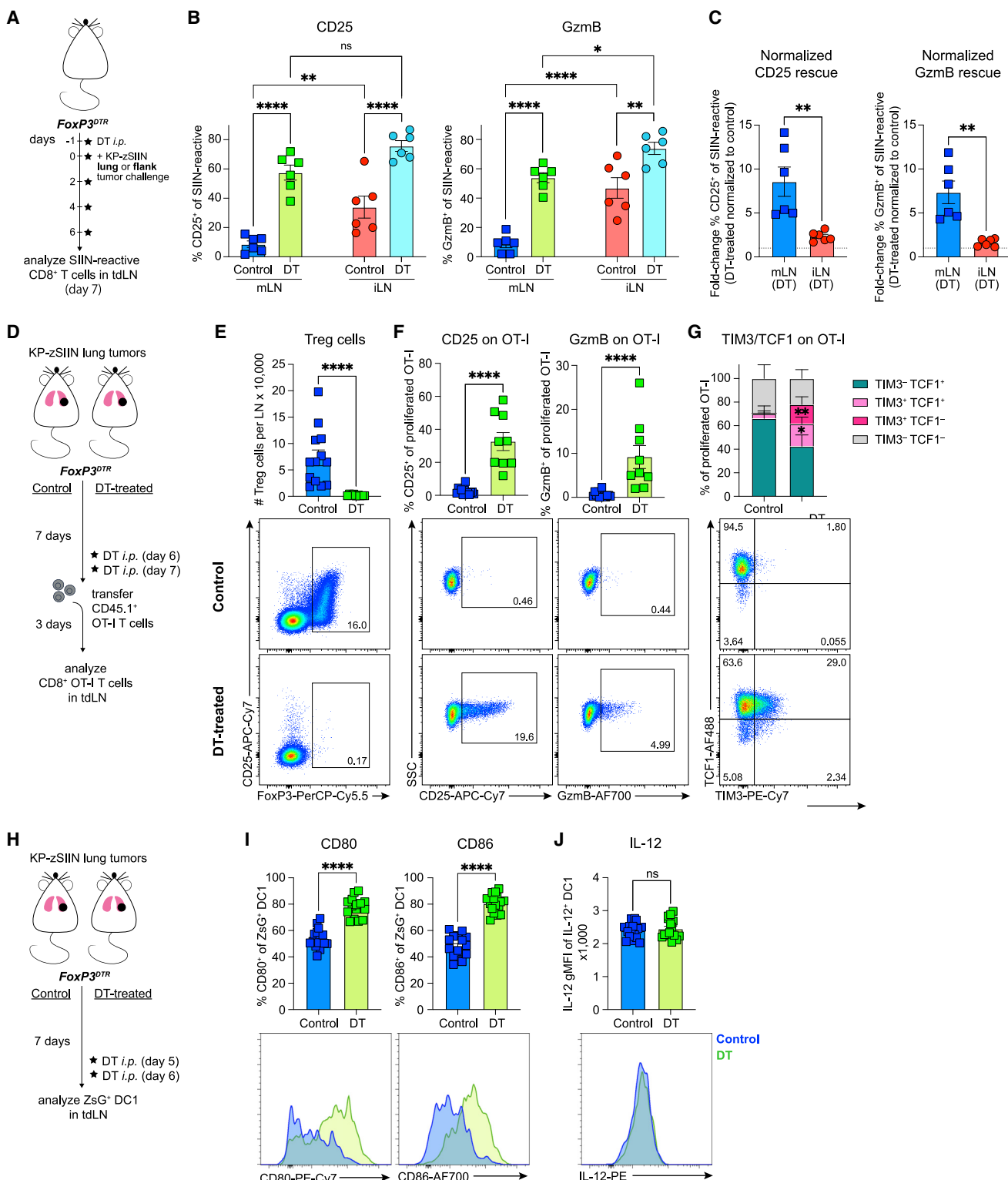


Figure 3. Treg cells can induce CD8⁺ T cell dysfunction and DC1 suppression in the tumor-draining mLN

(A) Experimental design for (B–C).

(B–C) Quantification of (B) CD25 and GzmB expression and (C) DT-treated/control ratios of CD25 and GzmB expression within each tdLN site for SIIN-reactive CD8⁺ T cells from control or DT-treated tumor-bearing *FoxP3^{DTR}* mice, day 7 post-tumor implantation (n = 3 mice/group; two independent experiments).

(D) Experimental design for (E–G).

(legend continued on next page)

expression of CD25 and GzmB ex vivo (Figures S1Y and S1Z). Thus, the dysfunctional CD8⁺ T cell responses in the tumor-draining mLN did not result from DC1-intrinsic defects, but instead, a DC-extrinsic, mLN-specific, and tumor-dependent factor restrained CTL activation *in vivo*.

Treg cells can induce CD8⁺ T cell dysfunction and DC1 suppression

Treg cells can suppress DC stimulatory capacity by depleting surface molecules CD80 and CD86.^{34,35,37–39} Given the low expression of CD80 and CD86 on ZsG⁺ DC1s from tumor-draining mLN (Figure 2D), we hypothesized that Treg cells inhibited DC1s and thereby caused dysfunctional CD8⁺ T cell responses in the mLN.

We used *FoxP3*^{DTR} mice⁵⁷ to examine the impact of constitutive Treg cell depletion on SIIN-reactive CD8⁺ T cell responses in the tumor-draining mLN and iLN (Figure 3A). Expression of CD25 and GzmB on tumor-reactive T cells was markedly increased upon Treg cell depletion in both LNs (Figure 3B). The rescue of both CD25 and GzmB expression on tumor-reactive T cells was greater in the mLN (Figure 3C), suggesting a more profound Treg cell suppression in the mLN compared with the iLN. While other tissue-specific suppressive factors cannot be fully excluded, these data provided a strong rationale to study the role of Treg cells in shaping the quality of tumor-specific T cell responses in the mLN.

As constitutive Treg cell ablation causes severe autoimmunity,⁵⁷ we further assessed the impact of transient Treg cell depletion. Transient depletion likewise restored CTL priming in the mLN (Figures 3D–3G). Transient Treg cell depletion also led to an increased expression of CD80 and CD86, but not IL-12, on ZsG⁺ DC1s from the mLN (Figures 3H–3J). Similar effects were observed in the iLN (Figures S1AA–S1AC). Therefore, Treg cells suppressed tumor-reactive T cell responses and DC1 stimulatory capacity in both LNs; however, their inhibition of CTL priming was more potent in the mLN.

Treg cells from the tumor-draining mLN restrain cytotoxic T cell priming by suppressing DC-derived signals 2 and 3

As DC1s were required for T cell priming in the mLN (Figure 1) and Treg cells suppressed CTL differentiation (Figure 3), we hypothesized that mLN Treg cells restrained CD8⁺ T cell priming by inhibiting DC1s. To delineate the effects of DC1s and Treg cells on CD8⁺ T cell priming, we utilized reductionist *ex vivo* co-cultures of naive OT-I T cells with ZsG⁺ DC1s and Treg cells isolated from the tumor-draining mLN (Figure 4A; see Methods for details). Treg cells caused a stark reduction in CD25 and GzmB expression on OT-I T cells at low Treg:OT-I T cell ratios (Figures 4B–4D), while CD8⁺ T cell proliferation was only mildly reduced (Figures 4D, S2A, and S2B). The resulting CD25^{low}

GzmB^{low} phenotype recapitulated the CD8⁺ T cell dysfunction phenotype observed *in vivo* (Figure 1E). To test whether Treg cells required DC1s to induce dysfunctional CD8⁺ T cells, we used plate-bound anti-(α)CD3 and α CD28 to stimulate OT-I T cells (Figure 4A). In the absence of DC1s, the same number of Treg cells minimally impacted CD25 and GzmB expression on OT-I T cells (Figures 4C and 4D). Thus, Treg cells could redirect DC1-mediated priming of CTLs toward dysfunction yet require the presence of DC1s for this suppression.

To ascertain whether CD8⁺ T cell states from the *ex vivo* co-cultures (ZsG⁺ DC1:OT-I \pm Treg cells, Figures 4A–4D) and the *in vivo* priming assay (mLN versus iLN, Figures 1D–1F) were comparable beyond phenotypic markers, we performed single-cell RNA sequencing (scRNA-seq) of *ex vivo*-primed T cells (Figure S2C). We examined the differentially expressed genes (DEGs) between CD8⁺ T cells primed by DC1s in the presence or absence of Treg cells (Figure S2D and Table S1). Treg cell presence led to reduced expression of transcripts associated with effector function (*GzmB*, *Il2ra*, *Il12rb1*, and *Il12rb2*) and increased expression of transcripts associated with inhibition of effector T cell differentiation (*Sell*, *Pecam1*, *Lef1*, *Tcf7l*, *S1pr1*, *S1pr4*) and T cell fate decisions (*Klf2*, *Klf3*) on CD8⁺ T cells^{24,58–64} (Figure S2D). The transcriptional profiles of T cells primed *ex vivo* in the presence or absence of Treg cells strongly correlated with the published RNA sequencing (RNA-seq)²⁴ of T cells primed *in vivo* in the KP-tumor-draining mLN or iLN, respectively (Figures S2E and S2F). This result indicated that transcriptional differences between mLN- and iLN-primed T cells were largely conserved in T cells primed *ex vivo*.

Next, we directly compared the functional suppressive capacity of mLN and iLN Treg cells. Consistent with the *in vivo* Treg cell depletion data (Figures 3A–3C), both mLN and iLN Treg cells inhibited CD25 and GzmB expression on primed CD8⁺ T cells (Figures 4E–4G). However, mLN Treg cells induced more potent suppression than iLN Treg cells, regardless of whether ZsG⁺ DC1s were isolated from the mLN or iLN (Figures 4E–4G, S2G, and S2H). Tissue-specific differences in Treg cell-intrinsic suppressive capacity were only detectable in the DC1:Treg:OT-I T cell co-cultures, as the α CD3/ α CD28-based co-cultures revealed comparable suppression (Figures S2I and S2J).

To compare DC suppression effects of mLN and iLN Treg cells in a controlled setting, we established co-cultures of mature bone marrow-derived-DCs (BM-DCs) derived from *p40*-IRESeYFP IL-12 reporter mouse bone marrow and Treg cells sorted from the tumor-draining mLN and iLN (Figure 4H; see Methods for details). Consistent with the *in vivo* data (Figures 2D, 3I, and S1AB), both mLN and iLN Treg cells suppressed CD80 and CD86 expression on BM-DCs (Figures 4I and 4J). However, mLN Treg cells inhibited CD80 and CD86 expression more effectively (Figures 4I and 4J), mirroring *in vivo* differences in DC1 costimulatory molecule expression in the mLN and iLN (Figure 2D).

(E–G) Representative flow plots and quantified (E) Treg cell number, (F) expression of CD25, GzmB, (G) TCF1, and TIM-3 on adoptively transferred proliferated OT-I T cells from mLNs of control or DT-treated tumor-bearing *FoxP3*^{DTR} mice, day 10 post-tumor implantation (n = 2–4 mice/group; four independent experiments).

(H) Experimental design for (I–J).

(I–J) Representative histograms and quantified expression of (I) CD80, CD86, and (J) IL-12 on ZsG⁺ DC1s from mLNs of control or DT-treated tumor-bearing *FoxP3*^{DTR} mice, day 7 post-tumor implantation (mLNs from 3 to 5 mice pooled per datapoint; six independent experiments).

*p < 0.05, **p < 0.01, ***p < 0.0001, ns = not significant; two-way ANOVA (B), MWU (C, E–G, I–J). Data shown as mean \pm SEM.

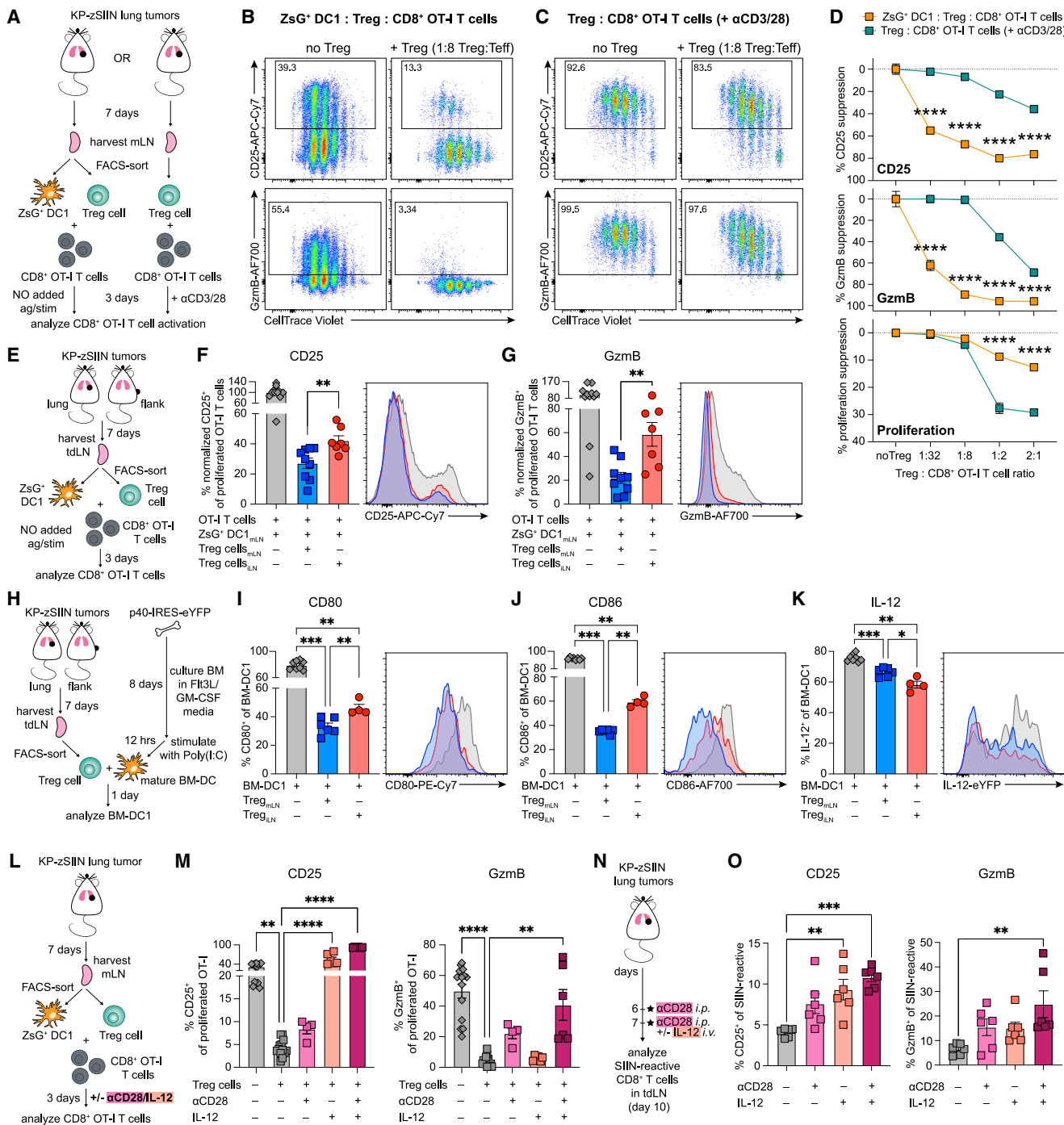


Figure 4. Treg cells from the tumor-draining mLN restrain cytotoxic T cell priming by suppressing DC-derived signals 2 and 3

(A) Experimental design for (B–D).

(B–D) Representative flow plots of proliferation, CD25, and GzmB expression of CTV-labelled OT-I T cells after 3-day co-culture with (B) mLN-sorted ZsG⁺ DC1s and Treg cells or (C) mLN-sorted Treg cells with αCD3/αCD28-stimulation; representative example quantified in (D) (50 tdLNs pooled for sorting, three independent experiments).

(E) Experimental design for (F–G).

(F–G) Representative histograms and quantified expression of (F) CD25 and (G) GzmB on proliferated OT-I T cells after 3-day co-culture with mLN-sorted ZsG⁺ DC1s and either mLN- or iLN-sorted Treg cells (50 tdLNs pooled for sorting, three independent experiments).

(H) Experimental design for (I–K).

(I–K) Representative histograms and quantified expression of (I) CD80, (J) CD86, and (K) IL-12 on p40-IRES-eYFP BM-DC1s after 3-day co-culture with either mLN- or iLN-sorted Treg cells (15 tdLNs pooled for sorting, two independent experiments).

(legend continued on next page)

Treg cells from the iLN induced increased IL-12 suppression compared with Treg cells from the mLN (Figure 4K), which contrasts with the *in vivo* observation (Figure 2E). This discrepancy could be explained by a lack of effector T cells in this assay as T cell-derived IFN- γ induces IL-12 expression.⁶⁵

Insufficiency of DC-derived stimulatory signals can prevent differentiation of CTLs.^{18,19,31} If Treg cell-mediated inhibition of signals 2 and 3 on DC1s caused dysfunctional priming of CD8⁺ T cells in the mLN, then providing signals 2 and 3 exogenously should restore CTL priming. Using ZsG⁺ DC1:Treg:OT-I T cell co-cultures, we found that singular addition of α CD28 (signal 2) or IL-12 (signal 3) induced a partial increase of GzmB and high expression of CD25, respectively (Figures 4L–M). However, combining α CD28 and IL-12 led to a synergic effect, completely restoring both GzmB and CD25 expression (Figure 4M). We then examined the impact of α CD28 and IL-12 treatment on CD8⁺ T cell priming in the mLN of lung tumor-bearing mice (Figure 4N). Consistent with *ex vivo* results, we observed that the combination of α CD28 and IL-12 induced robust CD25 and GzmB expression on the tumor-reactive CD8⁺ T cells (Figure 4O). Thus, Treg cells in the tumor-draining mLN caused dysfunctional priming of CD8⁺ T cells due to an enhanced ability to suppress DC1 stimulatory signals.

Treg cells suppress CD8⁺ T cell priming in the mLN via direct interaction with DC1s

Treg cells can suppress DC stimulatory molecules in a contact-dependent or contact-independent manner.^{34,35} To first evaluate the spatial arrangement of Treg cells and DC1s during CD8⁺ T cell priming, we performed immunofluorescence (IF) staining of tumor-draining mLNs and iLNs from *XCR1^{DTR}.Venus* mice after adoptive transfer of CD45.1⁺ OT-I T cells (Figure 5A). We identified XCR1⁺ DC1s, tumor-reactive OT-I T cells, and Treg cells using the endogenous Venus signal, CD45.1, and FoxP3 markers, respectively (Figure 5B; see Methods for details). We focused our analysis on the OT-I T cell microniches, defined as circular regions centered at OT-I T cell clusters that contain at least one DC1 (Figure 5B; see Methods for details), and evaluated Treg:DC1 proximity by measuring the distance from each Treg cell to its closest DC1. The microniche-associated Treg cells and DC1s were closer to each other in the tumor-draining mLN compared with the iLN (Figures 5B, 5C, and S2K). This spatial proximity of Treg cells and DC1s in the mLN was a microniche-specific effect, because outside of microniches, the Treg:DC1 distance was increased (Figure 5C). Microniches in the mLN and iLN were similar in size, and the Treg:DC1 ratio within microniches was also not increased in the mLN (Figure 5D). Increased Treg cell suppression in the mLN was likely driven by the physical proximity of Treg cells and DC1s involved in tumor-specific CD8⁺ T cell activation.

To test whether Treg cell-mediated suppression of DC1s required direct cell:cell contact, we abrogated their MHC-II-dependent interactions. Antibody-mediated MHC-II blockade in *ex vivo* ZsG⁺ DC1:Treg:OT-I T cell co-cultures completely reversed the Treg cell suppression phenotype (Figures 5E and 5F), suggesting that MHC-II accessibility on DC1s was critical for the Treg cell-mediated suppression of CD8⁺ T cell priming. To test the effect of MHC-II ablation on DC1 stimulatory capacity *in vivo*, we generated wild-type WT:*H2-Ab1^{-/-}* mixed bone marrow chimeras (BMCs) and compared the phenotypes of wild type (WT) and *H2-Ab1^{-/-}* ZsG⁺ DC1s within the tumor-draining mLN (Figures 5G, S2L, and S2M). MHC-II deletion resulted in increased expression of CD80, CD86, and IL12 on ZsG⁺ DC1s *in vivo* (Figures 5H and 5I), indicating that Treg cell-mediated suppression effects were conferred to DC1s through MHC-II-dependent interactions.

We then examined the impact of DC1-specific MHC-II deletion on CD8⁺ T cell priming *in vivo*. We generated WT, *Batf3^{-/-}:WT*, and *Batf3^{-/-}:H2-Ab1^{-/-}* mixed BMCs to compare the effect of MHC-II⁺ DC1s (in WT and *Batf3^{-/-}:WT* BMCs) and MHC-II⁻ DC1s (in *Batf3^{-/-}:H2-Ab1^{-/-}* BMCs) on CD8⁺ T cell priming (Figures 5J, S2N, and S2O). DC1-specific MHC-II deletion in *Batf3^{-/-}:H2-Ab1^{-/-}* BMCs restored the priming of CTLs in the mLN compared with control BMCs (Figure 5K). We independently validated this result using *XCR1^{DTR}:WT* and *XCR1^{DTR}:H2-Ab1^{-/-}* mixed BMCs (Figures 5L, S2P, and S2Q). Consistently, the DC1-specific MHC-II deletion led to effective priming of CTLs in the tumor-draining mLN (Figure 5M). Therefore, MHC-II-dependent Treg:DC1 interactions caused DC1 suppression and the associated CD8⁺ T cell dysfunction in the context of lung tumors.

Th1-like Treg cells expand in tumor-draining mLNs

It remained unclear what tissue-specific factor(s) caused Treg cells to be more suppressive in the mLN compared with the iLN. Because increased suppression is often associated with a greater Treg cell abundance,^{66,67} we enumerated Treg cells in both tdLNs. However, Treg cells were equally abundant (Figures 6A and 6B), and SIIN-reactive CD8⁺/Treg cell ratios did not correlate with increased suppression observed in the tumor-draining mLN (Figure S3A).

Treg cells are heterogeneous and have distinct tissue-specific functional specializations and TCR repertoires,⁶⁸ which could influence their suppressive capacity. To characterize their transcriptional states, we performed scRNA-seq paired with T cell receptor sequencing (TCR-seq) on Treg cells sorted from mLNs and iLNs of tumor-bearing and naive mice (Figure 6C). We obtained high-quality transcriptomes for 16,249 Treg cells (Figure S3B) and recovered TCR- β sequences from 55.4% of cells, TCR- α sequences from 23.1% of cells, and paired TCR- β and TCR- α sequences from 14.4% of cells (Figures S3C and

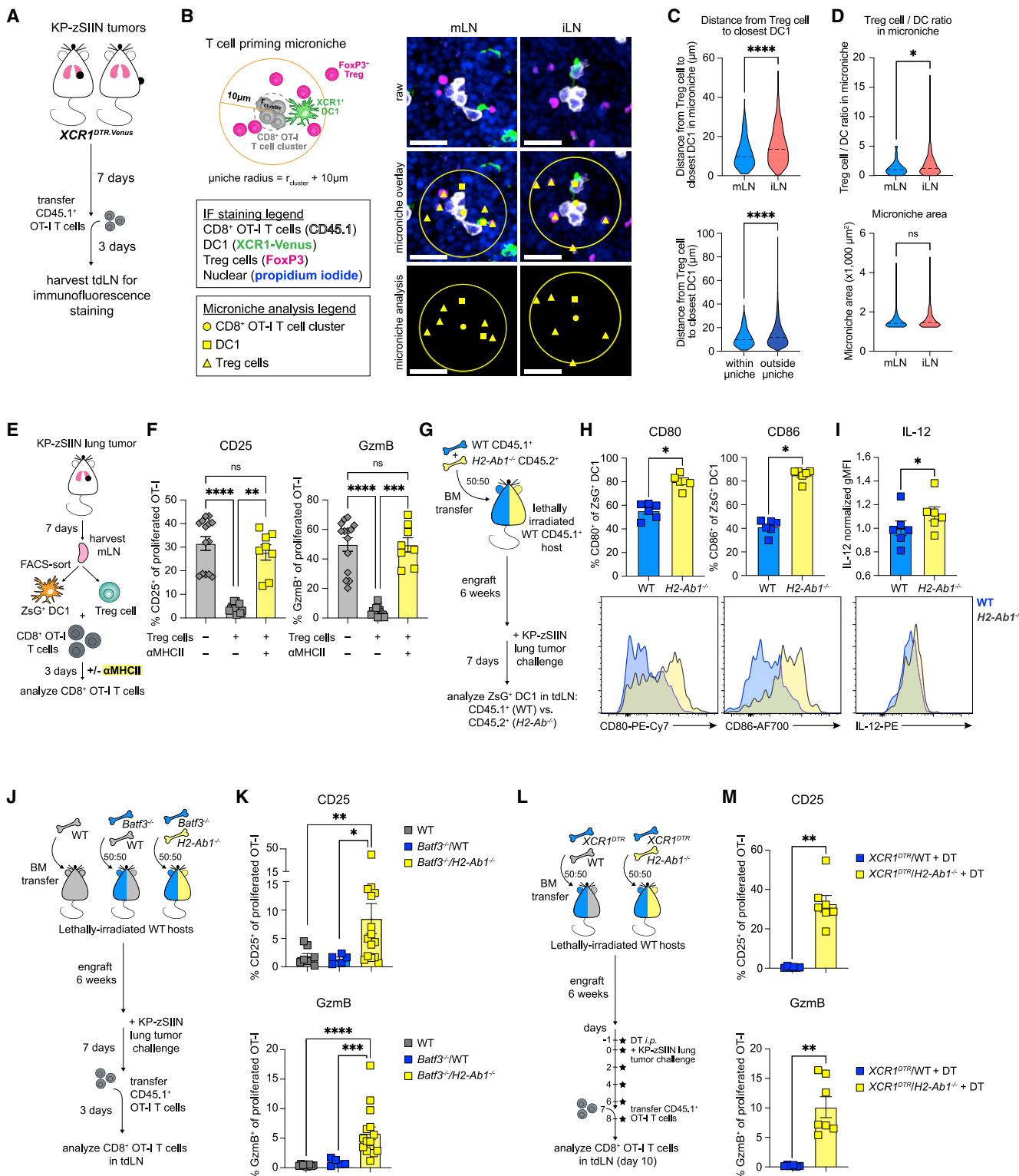
(L) Experimental design for (M).

(M) CD25 and GzmB expression on proliferated OT-I T cells after 3-day co-culture with mLN-sorted DC1s and Treg cells at indicated culture conditions (50 mLNs pooled for sorting, four independent experiments).

(N) Experimental design for (O).

(O) CD25 and GzmB expression on SIIN-reactive CD8⁺ T cells in tumor-draining mLNs, day 10 post-tumor implantation ($n = 3$ mice/group; two independent experiments).

* $p < 0.05$, ** $p < 0.01$, *** $p < 0.001$, **** $p < 0.0001$; two-way ANOVA (D), MWU (F–G, I–K) or Kruskal-Wallis test (KW) (M, O). Data shown as mean \pm SEM.

**Figure 5. Treg cells suppress CD8⁺ T cell priming in the mLN via direct interaction with DC1s**

(A) Experimental design for (B)–(D) and Figure S2K.

(B) Schematic of microniche analysis for (C–D) and representative IF images of tdLNs from tumor-bearing XCR1^{DTR.Venus} mice, day 10 post-tumor implantation; scale bar, 20 μ m.

(legend continued on next page)

S3D). Initial unsupervised analysis identified four clusters of Treg cells, and we focused subsequent analysis on three clusters of activated Treg cells that exhibited reduced expression of markers and gene sets associated with naive T cells (Figures S3E–S3I).^{69–71} Among activated Treg cells, we identified four clusters, including Treg cells enriched for transcripts associated with early activation (*Nr4a1*, *Egr1*, *Egr2*, *Myc*, *Dusp*), proliferation (*Mki67*, *Top2a*, *Stmn1*, *Cenpf*, *Birc5*), and two activated Treg cell clusters (activated cluster 1 [c1]: *Cxcr3*, *Icos*, *Tigit*, *Prdm1*, *Ctla4*; activated c2: *Rorc*, *Ccr6*, *Il10ra*, *Il18r1*, *Tgfbr2*) (Figures 6D and 6E and Table S2).^{72,73} Activated c1 Treg cells were markedly enriched in both tdLN compared with the naive LN, suggesting that this transcriptional program was induced in response to tumor (Figure S3J). As Treg cells can suppress in an antigen-specific manner^{74,75} and expand clonally in response to tumors,^{76–78} we evaluated their clonal expansion. Treg cells expanded clonally in both tdLN but not in either of the naive LNs (Figures 6F and 6G). The degree of overall clonal expansion was comparable between tumor-draining mLN and iLN and restricted to the activated c1 Treg cell cluster (Figures 6F and 6G).

To evaluate Treg cell specificity, we analyzed CDR3 sequences within activated c1 Treg cells. Four public TCR-β sequences were recovered independently from Treg cells in multiple mice and shared across mLN and iLN (Table S3). These sequences were often formed by distinct nucleotide rearrangements, demonstrating a convergence in the TCR repertoire (Table S3). These sequences were much more likely to exhibit clonal expansion than other CDR3-β sequences (Figure S3K) and were entirely absent from the naive iLN or mLN (Table S3), despite a comparable degree of sequence recovery (Figures S3C and S3D). These data suggested that the Treg cells analyzed here were responsive toward tumor-associated antigens present in both tdLN. While these data did not exclude the possibility that TCR repertoire differences could affect Treg cell suppressive capacity, they suggested that features other than the TCR might be dominant in mediating Treg cell suppressive functions.

The phenotype of activated c1 Treg cells correlated with increased functional suppression capacity (Figures S3L and S3M), which prompted us to interrogate transcriptional differences in activated c1 Treg cells from the mLN and iLN (Figure 6H and Table S4). Activated c1 Treg cells from the mLN differentially

expressed transcripts associated with immunosuppression (*Nrp1*, *Fgl2*, and *Nt5e*),^{79–81} IFN response, and Th1 polarization (*Ifngr1*, *Cxcr3*, *Tbx21*, *Cybb*, and *Ptpn11*),^{82–84} while their iLN counterparts were enriched for transcripts associated with T cell activation (*Icos* and *Gcnt1*)^{85,86} and Treg cell survival and stability (*Cd2* and *Satb1*)^{87,88} (Figure 6H). Additionally, because Th2-like Treg cells can effectively suppress anti-tumor immunity,^{89,90} we examined expression of canonical Th1-, Th2-, and Th17-polarizing transcription factors (*Tbx21*, *Gata3*, and *Rorc*, respectively) on activated c1 Treg cells. Consistently, *Tbx21* expression was increased in the tumor-draining mLN of all analyzed mice, while *Gata3* and *Rorc* were similarly expressed (Figure S3N). Thus, activated c1 Treg cells were Th1 polarized in the tumor-draining mLN.

Further flow characterization of Treg cells in the two tdLN revealed increased expression of natural Treg cell markers neuropilin 1 (NRP1) and Helios and effector activation markers PD-1 and CTLA-4 on Treg cells from the mLN (Figures 6I, 6J, S4A, and S4B). Suppressive molecules NRP1, CTLA-4, CD39, and CD73 were differentially expressed on mLN Treg cells, while transforming growth factor beta 1 (TGF-β1) and CD25 were highly expressed on iLN Treg cells (Figures 6J and S4A–S4D), suggesting qualitatively distinct modes of suppression. Ki67 and FoxP3 expression was similar (Figure S4E). Consistent with scRNA-seq results, Th1-like markers CXCR3 and T-bet were differentially expressed on mLN Treg cells (Figure 6K). Analysis of T-bet, Gata3, and RORγt expression confirmed the Th1 polarization, as T-bet was most highly expressed on both bulk and CD44⁺ CD62L⁻ effector Treg (eTreg) cells in the mLN compared with the iLN (Figures 6L and S4F), and the frequency of T-bet⁺ CXCR3⁺ Th1-like eTreg cells was increased in the mLN (Figure S4G). Treg cells in the mLN acquired a Th1-like effector phenotype enriched in a distinct set of suppression molecules.

As Treg cells directly interacted with DC1s in the mLN (Figure 5), we tested whether DC1s regulated the Treg cell response. While Treg cells expressed PD-1 and CTLA-4 similarly in WT and *Batf3*^{-/-} mice, T-bet was decreased and the frequency of T-bet⁺ CXCR3⁺ Th1-like eTreg cells was reduced in the absence of DC1s (Figures S4H–S4L). Thus, DC1s were required for the Th1 polarization of eTreg cells in the mLN.

Since IFN-regulated transcripts and proteins were preferentially expressed on Treg cells from the mLN compared with the iLN (Figures 6H, 6K, 6L, S4F, and S4G), we hypothesized that

(C–D) Distance from Treg cell to closest DC1 (C, top) within microneche in tumor-draining mLN and iLN or (C, bottom) in mLN within and outside of microneche, (D, top) Treg/DC1 ratio within microneche, and (D, bottom) microneche area in tdLN; using microneche radius: $r_{\text{cluster}} + 10\mu\text{m}$ (n = 4 mice/group including 399 mLN microneches and 74 iLN microneches; representative data from one of two independent experiments).

(E) Experimental design for (F).

(F) CD25 and GzmB expression on proliferated OT-I T cells after 3-day co-culture with mLN-sorted ZsG⁺ DC1s and Treg cells at indicated culture conditions (50 mLN pooled for sorting, four independent experiments); controls (gray bars) are the same as shown in Figure 4M.

(G) Experimental design for (H–I) and Figures S2L–M.

(H–I) Representative histograms and quantified expression of (H) CD80, CD86, and (I) IL-12 on WT and *H2-Ab1*^{-/-} ZsG⁺ DC1s from mLN of tumor-bearing WT/*H2-Ab1*^{-/-} BMCs, day 7 post-tumor implantation (mLN from 3 to 4 mice pooled per datapoint; two independent experiments).

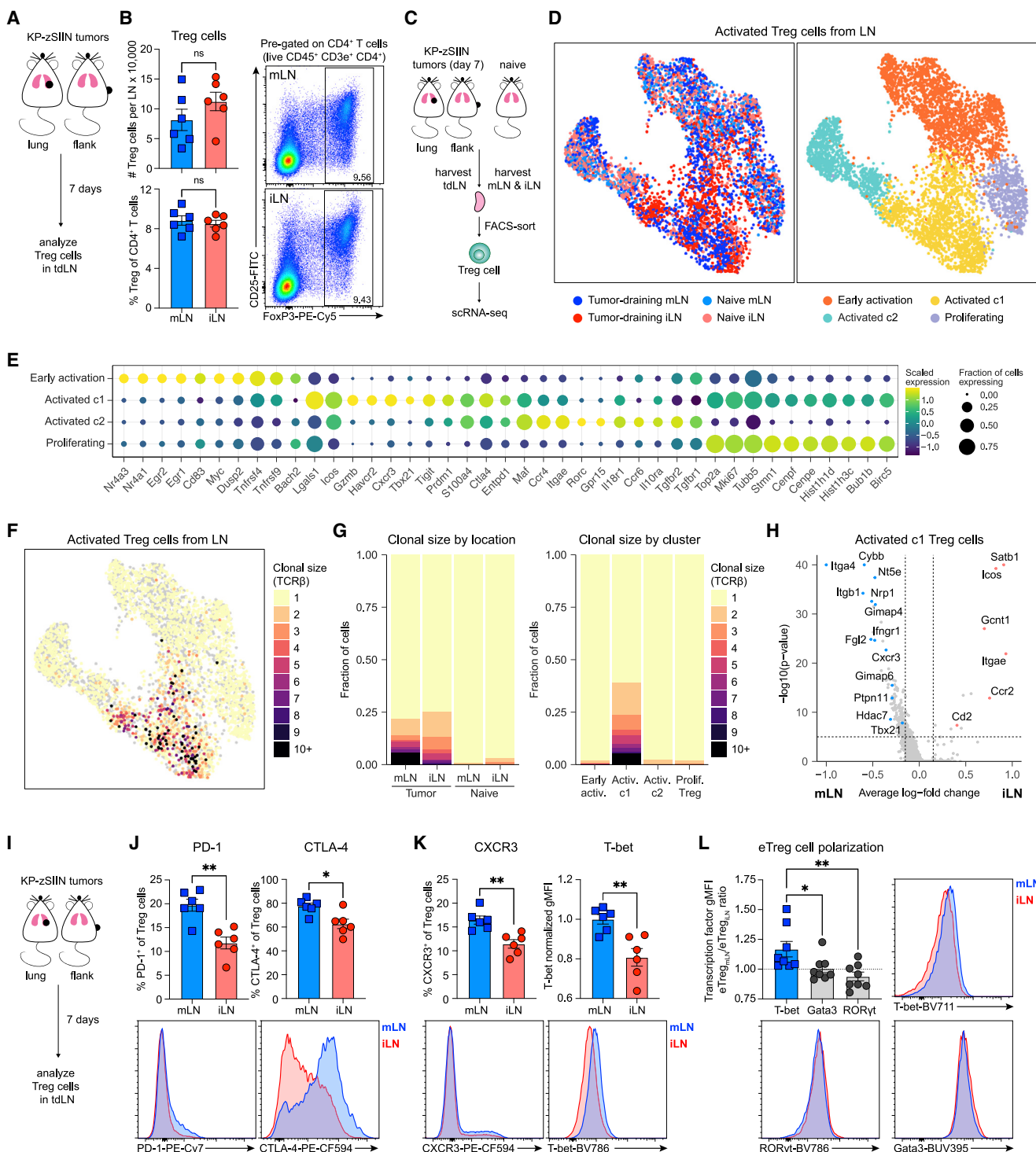
(J) Experimental design for (K) and Figures S2N–O.

(K) CD25 and GzmB expression on adoptively transferred proliferated OT-I T cells primed in mLN of tumor-bearing WT, *Batf3*^{-/-}/WT, or *Batf3*^{-/-}/*H2-Ab1*^{-/-} BMCs, day 10 post-tumor implantation (n = 2–5 mice/group; 1–4 independent experiments).

(L) Experimental design for (M) and Figures S2P–Q.

(M) CD25 and GzmB expression on adoptively transferred proliferated OT-I T cells primed in mLN of DT-treated tumor-bearing *Xcr1*^{DTR}/WT or *Xcr1*^{DTR}/*H2-Ab1*^{-/-} BMCs, day 10 post-tumor implantation (n = 3–4 mice/group; two independent experiments).

*p < 0.05, **p < 0.01, ***p < 0.0001, ns = not significant; MWU test (C–D, K, M), paired MWU (H–I), or KW (F). Data shown as mean ± SEM.

**Figure 6. Th1-like Treg cells expand in tumor-draining mLNs**

- (A) Experimental design for (B) and Figure S3A.
- (B) Representative flow plots and quantified abundance of Treg cells in tdLN, day 7 post-tumor implantation ($n = 3$ mice/group; two independent experiments).
- (C) Experimental design for (D)–(H) and Figures S3B–S3K and S3N.
- (D) Uniform manifold approximation and projection (UMAP) plots of activated Treg cells from naive and tumor-draining mLNs and iLNs colored (left) by tumor status and location or (right) by cluster (tdLNs, $n = 5$ mice/group; naive LN, $n = 20$ mice/group).
- (E) Dot plot of select marker genes for each Treg cluster displaying average expression and frequency for each gene.

(legend continued on next page)

IFN sensing induced Th1-like Treg cells in the mLN. We used WT:*Ifnar1*^{-/-}, WT:*Ifngr1*^{-/-}, and WT:*Ifngr1*^{-/-}*Ifnar1*^{-/-} mixed BMCs^{91,92} to compare the phenotypes of WT and IFN receptor-deficient (knockout [KO]) Treg cells within the tumor-draining mLN (Figures 7A, S5A, and S5B). While *Ifnar1* deletion induced a modest reduction in T-bet and had no impact on CXCR3 expression on Treg cells, *Ifngr1* deletion caused a severe reduction of both T-bet and CXCR3 expression (Figures 7B and S5C), consistent with published data.⁸² Although FoxP3, CD25, PD-1, CTLA-4, and CD73 expression were unaffected by IFN receptor deletion, CD39 was reduced on *Ifngr1*-deficient Treg cells in the mLN (Figures S5D and S5E). Expression of Th1 markers and CD39 on Treg cells was largely dependent on IFN- γ sensing in the tumor-draining mLN.

We then tested whether induction of Th1-like eTreg cells similarly depended on IFN sensing in both tdLNs. We generated *FoxP3*^{DTR,eGFP}:*Ifnar1*^{-/-}, *FoxP3*^{DTR,eGFP}:*Ifngr1*^{-/-}, and *FoxP3*^{DTR,eGFP}:*Ifngr1*^{-/-}*Ifnar1*^{-/-} mixed BMCs using congenically labeled hosts and compared phenotypes of donor-derived WT and IFN receptor-deficient (KO) eTreg cells within the tumor-draining mLN and iLN (Figures S5F and S5G). These BMCs enabled us to exclude host-derived Treg cells and verify that these radio-resistant cells did not confound our analysis. Consistent with earlier analysis of bulk Treg cells (Figures 7B and S5C), eTreg cell expression of T-bet and CXCR3 in the mLN depended on IFN- γ sensing (Figures S5H and S5I). Similarly, *Ifngr1*, but not *Ifnar1*, ablation blunted T-bet and CXCR3 expression on eTreg cells in the tumor-draining iLN (Figures S5H and S5I). Although T-bet⁺ CXCR3⁺ Th1-like eTreg cells were preferentially enriched in the WT immune fraction of the mLN relative to the iLN (Figure S5J), as shown before (Figure S4G), their frequency was comparable between mLN and iLN when *Ifngr1* was ablated (Figure S5J). Hence, the Th1-like eTreg cell program was IFN- γ dependent in both LNs, but it was predominantly induced in Treg cells of the mLN.

Because induction of Th1-like eTreg cells relied on IFN- γ sensing, we hypothesized that the mLN-specific enrichment in Th1-like eTreg cells could result from a tissue-specific difference in IFN- γ abundance. Indeed, IFN- γ was 3.78-fold more enriched in the tumor-draining mLN compared with the iLN (Figures 7C and 7D). In contrast, IL-2 abundance was comparable between the two tdLNs (Figures S6A and S6B). Further, IFN- γ measurements from naive LNs mirrored those from tdLNs, as IFN- γ was more abundant in the mLN compared with matched iLNs of naive mice (Figures 7E and 7F). The mLN-specific enrichment in IFN- γ was independent of tumor presence and was determined by the anatomical location of the LN. As lung microbiome-dependent IFN signals can impact

lung-specific immunity,⁹⁴ we tested whether the tissue-specific differences in IFN- γ would be maintained in germ-free (GF) mice. Unlike in specific-pathogen-free (SPF) mice, the amount of IFN- γ in the mLN and matched iLNs of naive GF mice was equalized (Figure 7G). Therefore, observed mLN-specific abundance of IFN- γ was caused by the presence of commensal bacteria.

mLN-specific enrichment in IFN- γ drives induction of Th1-like Treg cells and the associated dysfunctional T cell responses against lung cancer

Treg cells in the mLN expressed the chemokine receptor CXCR3 (Figure 6K), which guides intranodal positioning of effector T cells and facilitates interactions with DCs.⁹⁵⁻⁹⁷ To test whether CXCR3 was functionally required for Treg cells to suppress CTL responses against lung tumors, we generated *FoxP3*^{DTR}:WT and *FoxP3*^{DTR}:*Cxcr3*^{-/-} mixed BMCs. We treated both groups with diphtheria toxin (DT) to compare the suppressive effects of CXCR3-deficient Treg cells (in *FoxP3*^{DTR}:*Cxcr3*^{-/-} BMCs) and WT Treg cells (in *FoxP3*^{DTR}:WT BMCs) on CD8⁺ T cell priming (Figure S6C). Treg cell-specific deletion of CXCR3 has no impact on the CD8⁺ T cell phenotype in the tumor-draining mLN (Figures S6D and S6E), suggesting that several redundant chemokine receptor/ligand pathways might promote Treg:DC communication.⁹⁸⁻¹⁰⁰

As IFN- γ cytokine and IFN- γ -dependent Th1-like Treg cells were enriched in the mLN (Figures 6K, 6L, 7A–7F, S5C, and S5H–S5J), we tested whether IFN- γ sensing could regulate Treg cell ability to suppress CTL priming. We generated *FoxP3*^{DTR}:WT and *FoxP3*^{DTR}:*Ifngr1*^{-/-} mixed BMCs and treated the mice with DT to evaluate the impact of the *Ifngr1*-deficient Treg cells (in *FoxP3*^{DTR}:*Ifngr1*^{-/-} BMCs) or WT Treg cells (in *FoxP3*^{DTR}:WT BMCs) on CD8⁺ T cell priming in the tumor-draining mLN (Figures S6F and S6G). Compared with the control, *Ifngr1* ablation on Treg cells led to increased CD25 expression on CD8⁺ T cells primed in the mLN (Figures 7H and 7I). This 2.24-fold increase (± 0.374 SEM) (Figures 7H and 7I) was comparable to the 3.32-fold difference in CD25 expression (± 0.947 SEM) between iLN- and mLN-primed T cells (Figure 1E). Although GzmB and TIM3/TCF1 expression was unchanged (Figures 7I and S6H), the partial rescue was encouraging, as roughly half of all immune cells in *FoxP3*^{DTR}:*Ifngr1*^{-/-} BMCs were *Ifngr1* deficient, including DC1s, which depend on IFN- γ for IL-12 production.^{54,65} In the absence of DT treatment, CD8⁺ T cells primed in the mLN of *FoxP3*^{DTR}:WT and *FoxP3*^{DTR}:*Ifngr1*^{-/-} BMCs exhibited unchanged CD25 expression (Figures S6I–S6K), indicating that the observed rescue effect (Figure 7I) was driven by Treg cell-specific ablation of IFN- γ sensing.

(F–G) Clonal size of activated Treg cells (F) mapped onto UMAP plot and (G) graphed using stacked bar plots arranged (left) by tumor status and location or (right) by cluster.

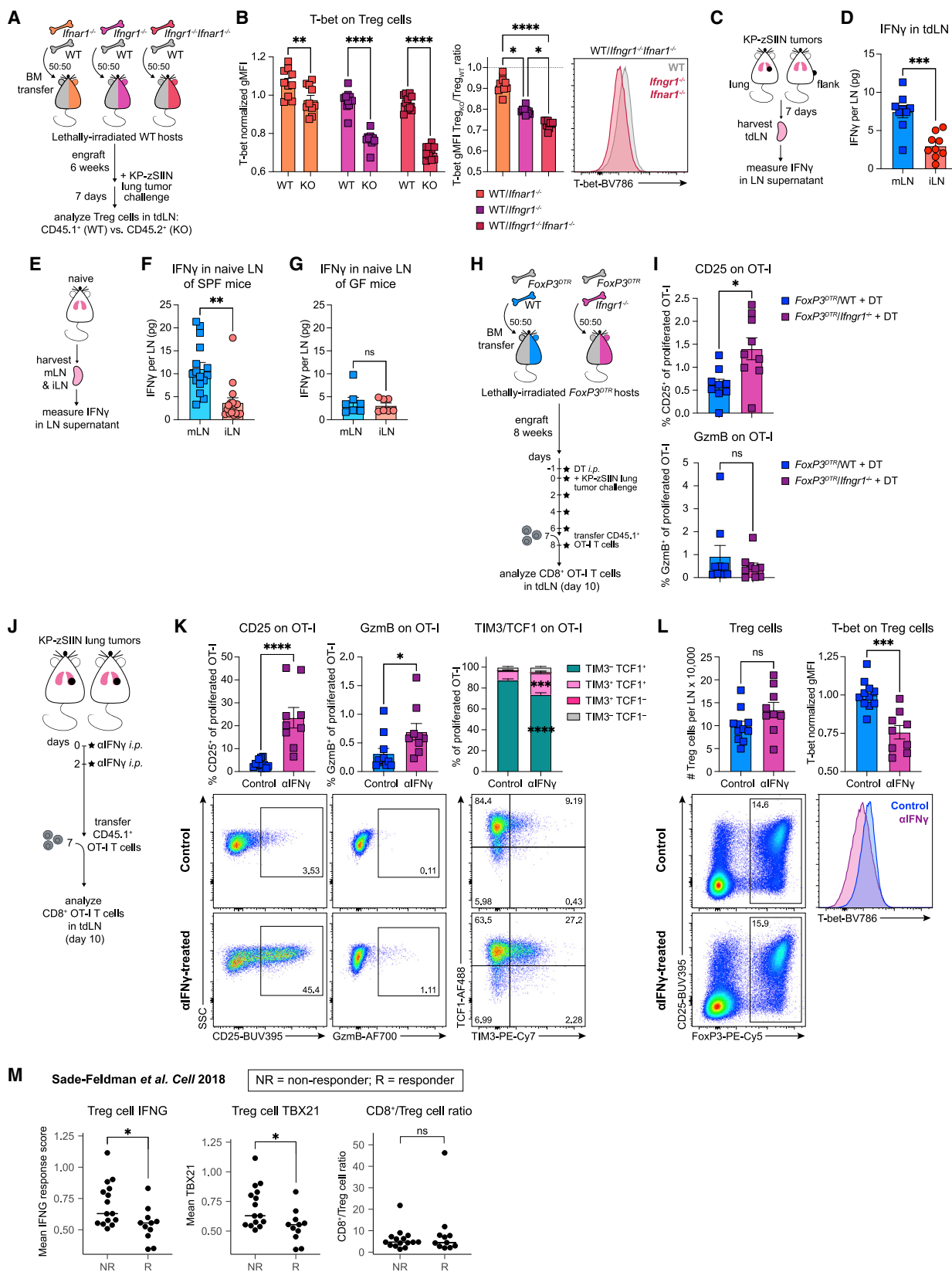
(H) Volcano plot of DEGs between activated c1 Treg cells from mLNs and iLNs.

(I) Experimental design for (J–L).

(J–K) Representative histograms and quantified expression of (J) PD-1, CTLA-4, (K) CXCR3, and T-bet on Treg cells from tdLNs, day 7 post-tumor implantation (n = 3 mice/group; two independent experiments).

(L) Representative histograms and transcription factor gMFI ratios for eTreg cells from tumor-draining mLNs and iLNs, day 7 post-tumor implantation (n = 4 mice/group; two independent experiments).

*p < 0.05, **p < 0.01, ns = not significant; MWU (B, J–L), MWU with Bonferroni correction (H). Data shown as mean \pm SEM.



(legend on next page)

We then evaluated whether antibody-mediated IFN- γ blockade could counter the IFN- γ -rich environment of the mLN and rewire Treg cell polarization and CD8 $^{+}$ T cell priming. Because IFN- γ plays an important role in CD8 $^{+}$ T cell effector differentiation,^{101–103} we administered IFN- γ blockade early post-tumor implantation and evaluated priming of adoptively transferred T cells (Figure 7J). IFN- γ blockade caused increased CD25, GzmB, and TIM-3 expression on the OT-I T cells in the tumor-draining mLN (Figure 7K) but had no impact in the tumor-draining iLN (Figures S7A and S7B), underscoring that this immunoregulation was tissue specific. Additionally, IFN- γ blockade caused decreased T-bet expression in both mLN and iLN Treg cells, while leaving the total number of Treg cells unchanged (Figures 7L and S7C). Transient IFN- γ blockade was sufficient to rescue CTL priming and alter the Treg cell phenotype in the IFN- γ -rich environment of the tumor-draining mLN.

To examine whether the IFN-dependent Th1-like Treg cells correlated with blunted anti-tumor immunity in humans, we reanalyzed a scRNA-seq dataset of tumor-infiltrating T cells from human melanoma.⁹³ Treg cell expression of the IFN response program and either TBX21 or CXCR3 transcripts strongly correlated with ICB resistance in these patients (Figures 7M and S7D). The CD8 $^{+}$ /Treg cell ratio did not associate with ICB response (Figure 7M), suggesting that the Treg cell quality, rather than quantity, determined anti-tumor immunity outcomes. Combined with our published finding that lung cancer-specific CD8 $^{+}$ T cell dysfunction drives ICB resistance,²⁴ these data suggested that IFN- γ -dependent Th1-like Treg cells correlated with ICB resistance in humans and mice.

DISCUSSION

We established that Th1-like eTreg cells in the lung tumor-draining mLN restrained activation of anti-tumor CTLs and induced a dysfunctional CD8 $^{+}$ T cell state. Mechanistically, Treg cells in the tumor-draining mLN suppressed DC1 stimulatory signals needed to drive successful CTL differentiation. The suppression was mediated via MHC-II-dependent contact between Treg cells

and DC1s and was associated with the mLN-specific Th1-like eTreg cell program characterized by increased T-bet and CXCR3 expression. Th1-like eTreg cells were induced by IFN- γ , which was preferentially enriched in the tumor-draining mLN. Antibody-mediated IFN- γ blockade could counter the naturally increased IFN- γ abundance in the mLN, resulting in Treg cell repolarization and enhanced CTL responses against lung tumors. Additionally, IFN- γ -induced Th1-like Treg cells correlated with ICB resistance in patients with cancer. Collectively, our data suggested that Th1-like eTreg cells acted on DC1s in the tdLN to prevent priming of CTL responses against lung tumors.

Mounting evidence suggests that the tissue site of tumor growth can influence anti-tumor immunity.^{104,105} By directly comparing T cell responses mounted against KP tumor cells implanted into the lungs or flanks of mice, we identified a Treg cell-driven lung-specific mechanism of immunosuppression. Lung tumor growth led to IFN- γ -dependent Th1-like eTreg responses associated with highly potent suppression capacity and enhanced spatial proximity to DC1s. These findings are consistent with prior reports describing the importance of IFN- γ -sensing Th1-like Treg cells for suppressing autoimmunity in type 1 diabetes and graft-versus-host disease.^{106–108} In addition to restraining CTL priming locally in the lung tdLN, we predict that this Treg cell state could systemically suppress anti-tumor immunity and potentially blunt secondary tumor control, as shown in prior studies.¹⁰⁹

We found that Th1-like eTreg cell responses in the lung setting were driven by the mLN-specific abundance in IFN- γ , which was induced by commensal bacteria. Consistent with our findings, the lung microbiome can directly impact lung-specific immuno-regulatory mechanisms¹¹⁰ as well as anti-tumor immunity.¹¹¹ The microbiome has further been reported to regulate the suppression capacity and frequency of Treg cells.^{112,113} Local immune populations that respond to commensal bacteria,¹¹⁴ such as unconventional T cells, have been described to migrate to the draining LN and shape conventional T cell responses in a tissue-specific manner.¹¹⁵ It remains to be determined which cells mediate the mLN-specific abundance in IFN- γ observed in this study.

Figure 7. mLN-specific enrichment in IFN- γ drives induction of Th1-like Treg cells and the associated dysfunctional T cell responses against lung cancer

- (A) Experimental design for (B).
- (B) Representative histogram and quantified T-bet expression on WT and IFN receptor-deficient (KO) Treg cells from mLNs of tumor-bearing WT/*Ifnar1*^{−/−}, WT/*Ifngr1*^{−/−}, or WT/*Ifngr1*^{−/−}/*Ifnar1*^{−/−} BMCs, day 7 post-tumor implantation (n = 5 mice/group; two independent experiments).
- (C) Experimental design for (D).
- (D) IFN- γ quantification in tdLNs, day 7 post-tumor implantation (n = 3 mice/group; three independent experiments).
- (E) Experimental design for (F–G).
- (F) IFN- γ quantification in LNs of naive SPF mice (n = 3–4 mice/group; five independent experiments).
- (G) IFN- γ quantification in LN of naive GF mice (n = 2–3 mice/group; three independent experiments).
- (H) Experimental design for (I).
- (I) CD25 and GzmB expression on adoptively transferred proliferated OT-I T cells primed in mLNs of DT-treated tumor-bearing *FoxP3*^{DTR}/WT or *FoxP3*^{DTR}/*Ifngr1*^{−/−} BMCs, day 10 post-tumor implantation (n = 3 mice/group; three independent experiments).
- (J) Experimental design for (K–L).
- (K–L) Representative flow plots and quantified expression of (K) CD25, GzmB, TIM3, and TCF1 on adoptively transferred proliferated OT-I T cells and (L) abundance and T-bet expression for Treg cells from mLNs of control and α IFN- γ -treated tumor-bearing mice, day 10 post-tumor implantation (n = 3–4 mice/group; three independent experiments).
- (M) Interferon gamma (IFNG) response hallmark signature scores and TBX21 expression on intratumoral Treg cells, along with CD8 $^{+}$ /Treg cell ratios in melanoma patients, including ICB responders (Rs) and ICB non-responders (NRs).⁹³
- *p < 0.05, **p < 0.01, ***p < 0.001, ****p < 0.0001, ns = not significant; two-way ANOVA (B, left) or KW (B, middle), paired-MWU (F–G), MWU (D, I, K–L, M). Data shown as mean \pm SEM, except in (M) where the median is shown.

Our observations do not exclude the possibility that Treg cell-independent tissue-specific factors might also contribute to the immunosuppressive microenvironment of the tumor-draining mLN. For instance, tumors from different anatomic sites differ in local nutrient availability,¹¹⁶ and the local metabolic environment directly regulates DC and T cell functions in cancer.^{117–121} It is plausible that differential nutrient availability in the tumor-draining iLN and mLN could further promote the qualitatively distinct T cell responses observed in our study.

Establishment of protective anti-tumor immunity requires a breach of immune tolerance;¹²² however, the mechanisms that maintain peripheral tolerance in cancer remain poorly understood. We uncovered a mechanism of MHC-II-dependent Treg cell-mediated DC1 suppression that restrained the activation of a protective anti-tumor T cell response in the tDLN. Th1-like eTreg cells were the critical mediators of this CD8⁺ T cell tolerance. Although we described this mechanism in the context of lung tumors, MHC-II ablation on DC1s can similarly disrupt peripheral tolerance of CD8⁺ T cells specific to a keratinocyte-derived self-antigen in the skin.¹²³ Thus, this peripheral tolerance mechanism is likely generalizable and not restricted to the lung setting. The preferential induction of peripheral tolerance in response to KP lung tumors, but not flank tumors, suggested that distinct tissue sites might have different tolerance setpoints. Because differential IFN- γ abundance regulated Treg cell phenotypes and suppression capacity, tissue-specific availability of cytokines might influence the tolerance setpoint in different contexts. Further research is needed to discern additional stimuli that regulate peripheral tolerance at different anatomic sites. An improved mechanistic understanding of peripheral tolerance regulation could inspire new therapeutic approaches to disrupt immune tolerance against cancer and boost protective anti-tumor immunity.

Limitations of the study

Our results strongly support the conclusion that IFN- γ sensing by Treg cells leads to enhanced suppression in the mLN. Refined studies utilizing mouse models that harbor Treg cell-specific *Ifngr1*^{-/-} are needed to fully elucidate the molecular mediators of this suppression. Additionally, it is important to further validate this immunoregulatory mechanism in the context of human biology using immune cell co-cultures and spatial analyses of Treg cells, DC1s, and CD8⁺ T cells in tDLNs of patients.

STAR★METHODS

Detailed methods are provided in the online version of this paper and include the following:

- KEY RESOURCES TABLE
- RESOURCE AVAILABILITY
 - Lead contact
 - Materials availability
 - Data and code availability
- EXPERIMENTAL MODEL AND SUBJECT DETAILS
 - Mice
 - Cell lines and tumor injections
- METHOD DETAILS

- Generation of expression vectors and modified tumor cell lines
- Adoptive transfer of T cells
- Tissue processing for flow cytometry, cell sorting and ELISpot
- Flow cytometry and FACS staining
- SIIN-tetramer staining
- *In vivo* mouse treatments
- IFN γ ELISpot
- Treg cell transcription factor analysis

● GENERATION OF BMC MICE

- *Ex vivo* T cell priming co-cultures
- Generation of BM-DC
- BM-DC:Treg cell co-cultures
- Tissue section preparation and immunostaining
- Imaging
- Image processing and spatial analysis
- Generation of IL-2 and IL-12 fusion proteins
- Cytokine measurements in LN supernatant
- Seq-Well scRNA-seq
- Processing of cell hashing data
- scRNA-seq data processing and visualization
- Paired single-cell TCR-seq and analysis
- Re-analysis of dataset from Sade-Feldman et al. (Cell 2018)

● QUANTIFICATION AND STATISTICAL ANALYSIS

SUPPLEMENTAL INFORMATION

Supplemental information can be found online at <https://doi.org/10.1016/j.immuni.2023.01.010>.

ACKNOWLEDGMENTS

We thank Ömer Yilmaz, Heaji Shin, and Andrea Vargas for providing GF mice; Arlene Sharpe (Harvard) and Max Krummel (UCSF) for advice; Ellen Duong, Yash Agarwal, Megan Ruhland (UCSF), Thomas Diefenbach (Ragon), and Peter Savage (UChicago) for experimental guidance; Arjun Bhutkar and Sarah Blatt for assistance with initial processing of the human dataset; Melissa Duquette for mouse colony maintenance and laboratory support; Paul Thompson for administrative support; and Koch Institute Swanson Biotechnology Center and the Ragon Institute Microscopy Core for technical support. This work was supported by the Pew Stewart scholarship, the Koch Institute Frontier Research program, the Ludwig Center at MIT, and in part by the MIT School of Science Fellowship in Cancer Research.

AUTHOR CONTRIBUTIONS

M.Z. and S.S. conceptualized the study. M.Z., B.L.H., E.T.-M., and S.S. designed experiments and interpreted data. M.Z., L.Y., D.M.M., and E.T.-M. performed experiments and analyzed data. A.E., C.V.M., and I.L.Z. conducted spatial analyses. M.Z., D.M.M., and A.E. developed methodology. N.M. and K.D.W. donated resources. J.G.F. supervised the study with germ-free mice. M.Z. and S.S. wrote the original draft. M.Z., L.Y., D.M.M., B.L.H., E.T.-M., A.E., and S.S. reviewed and edited the manuscript. S.S. and J.C.L. acquired funding. S.S. supervised the study.

DECLARATION OF INTERESTS

S.S. is a SAB member for Related Sciences, Arcus Biosciences, Ankyra Therapeutics, and Venn Therapeutics. S.S. is a co-founder of Danger Bio. S.S. is a consultant for TAKEDA, Merck, Tango Therapeutics, and Ribon Therapeutics and receives funding for unrelated projects from Leap Therapeutics. J.C.L. has interests in Sunflower Therapeutics PBC, Pfizer, Honeycomb Biotechnologies,

OneCyte Biotechnologies, SQZ Biotechnologies, Alloy Therapeutics, QuantumCyte, Amgen, and Repligen. S.S. and J.C.L.'s interests are reviewed and managed under MIT's policies for potential conflicts of interest. J.C.L. receives sponsored research support at MIT from Amgen, the Bill & Melinda Gates Foundation, Biogen, Pfizer, Roche, Takeda, and Sanofi.

Received: May 26, 2022

Revised: December 27, 2022

Accepted: January 11, 2023

Published: February 2, 2023

REFERENCES

- Fridman, W.H., Pagès, F., Sautès-Fridman, C., and Galon, J. (2012). The immune contexture in human tumours: impact on clinical outcome. *Nat. Rev. Cancer* 12, 298–306. <https://doi.org/10.1038/nrc3245>.
- Weigelin, B., den Boer, A.T., Wagena, E., Broen, K., Dolstra, H., de Boer, R.J., Figgdr, C.G., Textor, J., and Friedl, P. (2021). Cytotoxic T cells are able to efficiently eliminate cancer cells by additive cytotoxicity. *Nat. Commun.* 12, 5217. <https://doi.org/10.1038/s41467-021-25282-3>.
- Chen, D.S., and Mellman, I. (2013). Oncology meets immunology: the cancer-immunity cycle. *Immunity* 39, 1–10. <https://doi.org/10.1016/j.immuni.2013.07.012>.
- Hildner, K., Edelson, B.T., Purtha, W.E., Diamond, M., Matsushita, H., Kohyama, M., Calderon, B., Schraml, B.U., Unanue, E.R., Diamond, M.S., et al. (2008). Batf3 deficiency reveals a critical role for CD8alpha+ dendritic cells in cytotoxic T cell immunity. *Science* 322, 1097–1100. <https://doi.org/10.1126/science.1164206>.
- Broz, M.L., Binnewies, M., Boldajipour, B., Nelson, A.E., Pollack, J.L., Erle, D.J., Barczak, A., Rosenblum, M.D., Daud, A., Barber, D.L., et al. (2014). Dissecting the tumor myeloid compartment reveals rare activating antigen-presenting cells critical for T cell immunity. *Cancer Cell* 26, 938. <https://doi.org/10.1016/j.ccr.2014.11.010>.
- Lanzavecchia, A., and Sallusto, F. (2001). Regulation of T cell immunity by dendritic cells. *Cell* 106, 263–266. [https://doi.org/10.1016/s0092-8674\(01\)00455-x](https://doi.org/10.1016/s0092-8674(01)00455-x).
- den Haan, J.M., Lehar, S.M., and Bevan, M.J. (2000). CD8(+) but not CD8(-) dendritic cells cross-prime cytotoxic T cells in vivo. *J. Exp. Med.* 192, 1685–1696. <https://doi.org/10.1084/jem.192.12.1685>.
- De Plaen, E., Lurquin, C., Van Pel, A., Mariamé, B., Szikora, J.P., Wölfel, T., Sibille, C., Chomez, P., and Boon, T. (1988). Immunogenic (tum-) variants of mouse tumor P815: cloning of the gene of tum- antigen P91A and identification of the tum- mutation. *Proc. Natl. Acad. Sci. USA* 85, 2274–2278. <https://doi.org/10.1073/pnas.85.7.2274>.
- Inaba, K., Witmer-Pack, M., Inaba, M., Hathcock, K.S., Sakuta, H., Azuma, M., Yagita, H., Okumura, K., Linsley, P.S., Ikebara, S., et al. (1994). The tissue distribution of the B7-2 costimulator in mice: abundant expression on dendritic cells in situ and during maturation in vitro. *J. Exp. Med.* 180, 1849–1860. <https://doi.org/10.1084/jem.180.5.1849>.
- Caux, C., Vanbervliet, B., Massacrier, C., Azuma, M., Okumura, K., Lanier, L.L., and Banchereau, J. (1994). B70/B7-2 is identical to CD86 and is the major functional ligand for CD28 expressed on human dendritic cells. *J. Exp. Med.* 180, 1841–1847. <https://doi.org/10.1084/jem.180.5.1841>.
- Deeths, M.J., and Mescher, M.F. (1997). B7-1-dependent co-stimulation results in qualitatively and quantitatively different responses by CD4+ and CD8+ T cells. *Eur. J. Immunol.* 27, 598–608. <https://doi.org/10.1002/eji.1830270305>.
- Harding, F.A., McArthur, J.G., Gross, J.A., Raulet, D.H., and Allison, J.P. (1992). CD28-mediated signalling co-stimulates murine T cells and prevents induction of anergy in T-cell clones. *Nature* 356, 607–609. <https://doi.org/10.1038/356607a0>.
- Jenkins, M.K., Ashwell, J.D., and Schwartz, R.H. (1988). Allogeneic non-T spleen cells restore the responsiveness of normal T cell clones stimulated with antigen and chemically modified antigen-presenting cells. *J. Immunol.* 140, 3324–3330.
- Cella, M., Scheidegger, D., Palmer-Lehmann, K., Lane, P., Lanzavecchia, A., and Alber, G. (1996). Ligation of CD40 on dendritic cells triggers production of high levels of interleukin-12 and enhances T cell stimulatory capacity: T-T help via APC activation. *J. Exp. Med.* 184, 747–752. <https://doi.org/10.1084/jem.184.2.747>.
- Le Bon, A., Etchart, N., Rossmann, C., Ashton, M., Hou, S., Gewert, D., Borrow, P., and Tough, D.F. (2003). Cross-priming of CD8+ T cells stimulated by virus-induced type I interferon. *Nat. Immunol.* 4, 1009–1015. <https://doi.org/10.1038/ni978>.
- Curtsinger, J.M., Schmidt, C.S., Mondino, A., Lins, D.C., Kedl, R.M., Jenkins, M.K., and Mescher, M.F. (1999). Inflammatory cytokines provide a third signal for activation of naive CD4+ and CD8+ T cells. *J. Immunol.* 162, 3256–3262.
- Fuertes, M.B., Kacha, A.K., Kline, J., Woo, S.R., Kranz, D.M., Murphy, K.M., and Gajewski, T.F. (2011). Host type I IFN signals are required for antitumor CD8+ T cell responses through CD8 $\{\alpha\}$ + dendritic cells. *J. Exp. Med.* 208, 2005–2016. <https://doi.org/10.1084/jem.20101159>.
- Curtsinger, J.M., Lins, D.C., and Mescher, M.F. (2003). Signal 3 determines tolerance versus full activation of naive CD8 T cells: dissociating proliferation and development of effector function. *J. Exp. Med.* 197, 1141–1151. <https://doi.org/10.1084/jem.20021910>.
- Hernández, J., Aung, S., Marquardt, K., and Sherman, L.A. (2002). Uncoupling of proliferative potential and gain of effector function by CD8(+) T cells responding to self-antigens. *J. Exp. Med.* 196, 323–333. <https://doi.org/10.1084/jem.20011612>.
- Gett, A.V., Sallusto, F., Lanzavecchia, A., and Geginat, J. (2003). T cell fitness determined by signal strength. *Nat. Immunol.* 4, 355–360. <https://doi.org/10.1038/ni908>.
- van Stipdonk, M.J.B., Hardenberg, G., Bijker, M.S., Lemmens, E.E., Droin, N.M., Green, D.R., and Schoenberger, S.P. (2003). Dynamic programming of CD8+ T lymphocyte responses. *Nat. Immunol.* 4, 361–365. <https://doi.org/10.1084/ni912>.
- D'Souza, W.N., and Hedrick, S.M. (2006). Cutting edge: latecomer CD8 T cells are imprinted with a unique differentiation program. *J. Immunol.* 177, 777–781. <https://doi.org/10.4049/jimmunol.177.2.777>.
- Khan, O., Giles, J.R., McDonald, S., Manne, S., Ngiow, S.F., Patel, K.P., Werner, M.T., Huang, A.C., Alexander, K.A., Wu, J.E., et al. (2019). TOX transcriptionally and epigenetically programs CD8(+) T cell exhaustion. *Nature* 571, 211–218. <https://doi.org/10.1038/s41586-019-1325-x>.
- Horton, B.L., Morgan, D.M., Momin, N., Zagorulya, M., Torres-Mejia, E., Bhandarkar, V., Wittrup, K.D., Love, J.C., and Spranger, S. (2021). Lack of CD8(+) T cell effector differentiation during priming mediates checkpoint blockade resistance in non-small cell lung cancer. *Sci. Immunol.* 6, eabi8800. <https://doi.org/10.1126/sciimmunol.abi8800>.
- Zagorulya, M., and Spranger, S. (2022). Once upon a prime: DCs shape cancer immunity. *Trends Cancer*. <https://doi.org/10.1016/j.trecan.2022.10.006>.
- Romani, N., Koide, S., Crowley, M., Witmer-Pack, M., Livingstone, A.M., Fathman, C.G., Inaba, K., and Steinman, R.M. (1989). Presentation of exogenous protein antigens by dendritic cells to T cell clones. Intact protein is presented best by immature, epidermal Langerhans cells. *J. Exp. Med.* 169, 1169–1178. <https://doi.org/10.1084/jem.169.3.1169>.
- De Smedt, T., Pajak, B., Muraille, E., Lespagnard, L., Heinen, E., De Baetselier, P., Urbain, J., Leo, O., and Moser, M. (1996). Regulation of dendritic cell numbers and maturation by lipopolysaccharide in vivo. *J. Exp. Med.* 184, 1413–1424. <https://doi.org/10.1084/jem.184.4.1413>.
- Dalod, M., Salazar-Mather, T.P., Malmgaard, L., Lewis, C., Asselin-Paturel, C., Brière, F., Trinchieri, G., and Biron, C.A. (2002). Interferon alpha/beta and interleukin 12 responses to viral infections: pathways regulating dendritic cell cytokine expression in vivo. *J. Exp. Med.* 195, 517–528. <https://doi.org/10.1084/jem.20011672>.

29. Reis e Sousa, C., Hieny, S., Scharton-Kersten, T., Jankovic, D., Charest, H., Germain, R.N., and Sher, A. (1997). In vivo microbial stimulation induces rapid CD40 ligand-independent production of interleukin 12 by dendritic cells and their redistribution to T cell areas. *J. Exp. Med.* 186, 1819–1829. <https://doi.org/10.1084/jem.186.11.1819>.
30. Hawiger, D., Inaba, K., Dorsett, Y., Guo, M., Mahnke, K., Rivera, M., Ravetch, J.V., Steinman, R.M., and Nussenzweig, M.C. (2001). Dendritic cells induce peripheral T cell unresponsiveness under steady state conditions in vivo. *J. Exp. Med.* 194, 769–779. <https://doi.org/10.1084/jem.194.6.769>.
31. Bonifaz, L., Bonnyay, D., Mahnke, K., Rivera, M., Nussenzweig, M.C., and Steinman, R.M. (2002). Efficient targeting of protein antigen to the dendritic cell receptor DEC-205 in the steady state leads to antigen presentation on major histocompatibility complex class I products and peripheral CD8+ T cell tolerance. *J. Exp. Med.* 196, 1627–1638. <https://doi.org/10.1084/jem.20021598>.
32. Liu, K., Iyoda, T., Saternus, M., Kimura, Y., Inaba, K., and Steinman, R.M. (2002). Immune tolerance after delivery of dying cells to dendritic cells in situ. *J. Exp. Med.* 196, 1091–1097. <https://doi.org/10.1084/jem.20021215>.
33. Onishi, Y., Fehervari, Z., Yamaguchi, T., and Sakaguchi, S. (2008). Foxp3+ natural regulatory T cells preferentially form aggregates on dendritic cells in vitro and actively inhibit their maturation. *Proc. Natl. Acad. Sci. USA.* 105, 10113–10118. <https://doi.org/10.1073/pnas.0711106105>.
34. Gu, P., Gao, J.F., D’Souza, C.A., Kowalczyk, A., Chou, K.Y., and Zhang, L. (2012). Trogocytosis of CD80 and CD86 by induced regulatory T cells. *Cell. Mol. Immunol.* 9, 136–146. <https://doi.org/10.1038/cmi.2011.62>.
35. Qureshi, O.S., Zheng, Y., Nakamura, K., Attridge, K., Manzotti, C., Schmidt, E.M., Baker, J., Jeffery, L.E., Kaur, S., Briggs, Z., et al. (2011). Trans-endocytosis of CD80 and CD86: a molecular basis for the cell-extrinsic function of CTLA-4. *Science* 332, 600–603. <https://doi.org/10.1126/science.1202947>.
36. Mavin, E., Nicholson, L., Rafez Ahmed, S., Gao, F., Dickinson, A., and Wang, X.N. (2017). Human regulatory T cells mediate transcriptional modulation of dendritic cell function. *J. Immunol.* 198, 138–146. <https://doi.org/10.4049/jimmunol.1502487>.
37. Binnewies, M., Mujal, A.M., Pollack, J.L., Combes, A.J., Hardison, E.A., Barry, K.C., Tsui, J., Ruhland, M.K., Kersten, K., Abushawish, M.A., et al. (2019). Unleashing type-2 dendritic cells to drive protective anti-tumor CD4(+) T cell immunity. *Cell* 177, 556–571.e16. <https://doi.org/10.1016/j.cell.2019.02.005>.
38. Bauer, C.A., Kim, E.Y., Marangoni, F., Carrizosa, E., Claudio, N.M., and Mempel, T.R. (2014). Dynamic Treg interactions with intratumoral APCs promote local CTL dysfunction. *J. Clin. Invest.* 124, 2425–2440. <https://doi.org/10.1172/JCI66375>.
39. Marangoni, F., Zhakyp, A., Corsini, M., Geels, S.N., Carrizosa, E., Thelen, M., Mani, V., Prüßmann, J.N., Warner, R.D., Ozga, A.J., et al. (2021). Expansion of tumor-associated Treg cells upon disruption of a CTLA-4-dependent feedback loop. *Cell* 184, 3998–4015.e19. <https://doi.org/10.1016/j.cell.2021.05.027>.
40. Jang, J.E., Hajdu, C.H., Liot, C., Miller, G., Dustin, M.L., and Bar-Sagi, D. (2017). Crosstalk between regulatory T cells and tumor-associated dendritic cells negates anti-tumor immunity in pancreatic cancer. *Cell Rep.* 20, 558–571. <https://doi.org/10.1016/j.celrep.2017.06.062>.
41. Joshi, N.S., Akama-Garren, E.H., Lu, Y., Lee, D.Y., Chang, G.P., Li, A., DuPage, M., Tammela, T., Kerper, N.R., Farago, A.F., et al. (2015). Regulatory T cells in tumor-associated tertiary lymphoid structures suppress anti-tumor T cell responses. *Immunity* 43, 579–590. <https://doi.org/10.1016/j.immuni.2015.08.006>.
42. Poholek, A.C. (2021). Tissue-specific contributions to control of T cell immunity. *Immunohorizons* 5, 410–423. <https://doi.org/10.4049/immuno-horizons.2000103>.
43. Mikhak, Z., Strassner, J.P., and Luster, A.D. (2013). Lung dendritic cells imprint T cell lung homing and promote lung immunity through the chemokine receptor CCR4. *J. Exp. Med.* 210, 1855–1869. <https://doi.org/10.1084/jem.20130091>.
44. Kim, T.S., Gorski, S.A., Hahn, S., Murphy, K.M., and Braciale, T.J. (2014). Distinct dendritic cell subsets dictate the fate decision between effector and memory CD8(+) T cell differentiation by a CD24-dependent mechanism. *Immunity* 40, 400–413. <https://doi.org/10.1016/j.immuni.2014.02.004>.
45. Svensson, M., Johansson-Lindbom, B., Zapata, F., Jaensson, E., Austenaa, L.M., Blomhoff, R., and Agace, W.W. (2008). Retinoic acid receptor signaling levels and antigen dose regulate gut homing receptor expression on CD8+ T cells. *Mucosal Immunol.* 1, 38–48. <https://doi.org/10.1038/mi.2007.4>.
46. Esterházy, D., Canesso, M.C.C., Mesin, L., Muller, P.A., de Castro, T.B.R., Lockhart, A., ElJalby, M., Faria, A.M.C., and Mucida, D. (2019). Compartmentalized gut lymph node drainage dictates adaptive immune responses. *Nature* 569, 126–130. <https://doi.org/10.1038/s41586-019-1125-3>.
47. Mani, V., Bromley, S.K., Äijö, T., Mora-Buch, R., Carrizosa, E., Warner, R.D., Hamze, M., Sen, D.R., Chasse, A.Y., Lorant, A., et al. (2019). Migratory DCs activate TGF-beta to precondition naive CD8(+) T cells for tissue-resident memory fate. *Science* 366, eaav5728. <https://doi.org/10.1126/science.aav5728>.
48. Leal, J.M., Huang, J.Y., Kohli, K., Stoltzfus, C., Lyons-Cohen, M.R., Olin, B.E., Gale, M., Jr., and Gerner, M.Y. (2021). Innate cell microenvironments in lymph nodes shape the generation of T cell responses during type I inflammation. *Sci. Immunol.* 6, eabb9435. <https://doi.org/10.1126/sciimmunol.abb9435>.
49. Duckworth, B.C., Lafouresse, F., Wimmer, V.C., Broomfield, B.J., Dalit, L., Alexandre, Y.O., Sheikh, A.A., Qin, R.Z., Alvarado, C., Mielke, L.A., et al. (2021). Effector and stem-like memory cell fates are imprinted in distinct lymph node niches directed by CXCR3 ligands. *Nat. Immunol.* 22, 434–448. <https://doi.org/10.1038/s41590-021-00878-5>.
50. LaFave, L.M., Kartha, V.K., Ma, S., Meli, K., Del Priore, I., Lareau, C., Naranjo, S., Westcott, P.M.K., Duarte, F.M., Sankar, V., et al. (2020). Epigenomic state transitions characterize tumor progression in mouse lung adenocarcinoma. *Cancer Cell* 38, 212–228.e13. <https://doi.org/10.1016/j.ccr.2020.06.006>.
51. Roberts, E.W., Broz, M.L., Binnewies, M., Headley, M.B., Nelson, A.E., Wolf, D.M., Kaisho, T., Bogunovic, D., Bhardwaj, N., and Krummel, M.F. (2016). Critical role for CD103(+)CD141(+) dendritic cells bearing CCR7 for tumor antigen trafficking and priming of T cell immunity in melanoma. *Cancer Cell* 30, 324–336. <https://doi.org/10.1016/j.ccr.2016.06.003>.
52. Yamazaki, C., Sugiyama, M., Ohta, T., Hemmi, H., Hamada, E., Sasaki, I., Fukuda, Y., Yano, T., Nobuoka, M., Hirashima, T., et al. (2013). Critical roles of a dendritic cell subset expressing a chemokine receptor, XCR1. *J. Immunol.* 190, 6071–6082. <https://doi.org/10.4049/jimmunol.1202798>.
53. Duong, E., Fessenden, T.B., Lutz, E., Dinter, T., Yim, L., Blatt, S., Bhutkar, A., Wittrup, K.D., and Spranger, S. (2022). Type I interferon activates MHC class I-dressed CD11b(+) conventional dendritic cells to promote protective anti-tumor CD8(+) T cell immunity. *Immunity* 55, 308–323.e9. <https://doi.org/10.1016/j.immuni.2021.10.020>.
54. Maier, B., Leader, A.M., Chen, S.T., Tung, N., Chang, C., LeBerichel, J., Chudnovskiy, A., Maskey, S., Walker, L., Finnigan, J.P., et al. (2020). A conserved dendritic-cell regulatory program limits antitumour immunity. *Nature* 580, 257–262. <https://doi.org/10.1038/s41586-020-2134-y>.
55. Sallusto, F., Schaerli, P., Loetscher, P., Schaniel, C., Lenig, D., Mackay, C.R., Qin, S., and Lanzavecchia, A. (1998). Rapid and coordinated switch in chemokine receptor expression during dendritic cell maturation. *Eur. J. Immunol.* 28, 2760–2769. [https://doi.org/10.1002/\(SICI\)1521-4141\(199809\)28:09<2760::AID-IMMU2760>3.0.CO;2-N](https://doi.org/10.1002/(SICI)1521-4141(199809)28:09<2760::AID-IMMU2760>3.0.CO;2-N).
56. Cella, M., Engering, A., Pinet, V., Pieters, J., and Lanzavecchia, A. (1997). Inflammatory stimuli induce accumulation of MHC class II complexes on dendritic cells. *Nature* 388, 782–787. <https://doi.org/10.1038/42030>.

57. Fontenot, J.D., Gavin, M.A., and Rudensky, A.Y. (2003). Foxp3 programs the development and function of CD4+CD25+ regulatory T cells. *Nat. Immunol.* 4, 330–336. <https://doi.org/10.1038/ni904>.
58. Chen, Z., Ji, Z., Ngiow, S.F., Manne, S., Cai, Z., Huang, A.C., Johnson, J., Staupe, R.P., Bengsch, B., Xu, C., et al. (2019). TCF-1-centered transcriptional network drives an effector versus exhausted CD8 T cell-fate decision. *Immunity* 51, 840–855.e5. <https://doi.org/10.1016/j.immuni.2019.09.013>.
59. Pipkin, M.E., Sacks, J.A., Cruz-Guilloty, F., Lichtenheld, M.G., Bevan, M.J., and Rao, A. (2010). Interleukin-2 and inflammation induce distinct transcriptional programs that promote the differentiation of effector cytolytic T cells. *Immunity* 32, 79–90. <https://doi.org/10.1016/j.immuni.2009.11.012>.
60. Kalia, V., Sarkar, S., Subramaniam, S., Haining, W.N., Smith, K.A., and Ahmed, R. (2010). Prolonged interleukin-2Ralpha expression on virus-specific CD8+ T cells favors terminal-effector differentiation in vivo. *Immunity* 32, 91–103. <https://doi.org/10.1016/j.immuni.2009.11.010>.
61. Marelli-Berg, F.M., Clement, M., Mauro, C., and Caligiuri, G. (2013). An immunologist's guide to CD31 function in T-cells. *J. Cell Sci.* 126, 2343–2352. <https://doi.org/10.1242/jcs.124099>.
62. Xing, S., Li, F., Zeng, Z., Zhao, Y., Yu, S., Shan, Q., Li, Y., Phillips, F.C., Maina, P.K., Qi, H.H., et al. (2016). Tcf1 and Lef1 transcription factors establish CD8(+) T cell identity through intrinsic HDAC activity. *Nat. Immunol.* 17, 695–703. <https://doi.org/10.1038/ni.3456>.
63. Dorsam, G., Graeler, M.H., Serogy, C., Kong, Y., Voice, J.K., and Goetzl, E.J. (2003). Transduction of multiple effects of sphingosine 1-phosphate (S1P) on T cell functions by the S1P1 G protein-coupled receptor. *J. Immunol.* 171, 3500–3507. <https://doi.org/10.4049/jimmunol.171.7.3500>.
64. Hart, G.T., Hogquist, K.A., and Jameson, S.C. (2012). Kruppel-like factors in lymphocyte biology. *J. Immunol.* 188, 521–526. <https://doi.org/10.4049/jimmunol.1101530>.
65. Garris, C.S., Arlauckas, S.P., Kohler, R.H., Trefny, M.P., Garren, S., Piot, C., Engblom, C., Pfirsiche, C., Siwicki, M., Gungabeesoon, J., et al. (2018). Successful anti-PD-1 cancer immunotherapy requires T cell-dendritic cell crosstalk involving the cytokines IFN-gamma and IL-12. *Immunity* 49, 1148–1161.e7. <https://doi.org/10.1016/j.immuni.2018.09.024>.
66. Saleh, R., and Elkord, E. (2020). FoxP3(+) T regulatory cells in cancer: Prognostic biomarkers and therapeutic targets. *Cancer Lett.* 490, 174–185. <https://doi.org/10.1016/j.canlet.2020.07.022>.
67. Gubser, C., Schmalier, M., Rossi, S.W., and Palmer, E. (2016). Monoclonal regulatory T cells provide insights into T cell suppression. *Sci. Rep.* 6, 25758. <https://doi.org/10.1038/srep25758>.
68. Shevryev, D., and Tereshchenko, V. (2019). Treg heterogeneity, function, and homeostasis. *Front. Immunol.* 10, 3100. <https://doi.org/10.3389/fimmu.2019.03100>.
69. Miyara, M., Yoshioka, Y., Kitoh, A., Shima, T., Wing, K., Niwa, A., Parizot, C., Taflin, C., Heike, T., Valeyre, D., et al. (2009). Functional delineation and differentiation dynamics of human CD4+ T cells expressing the FoxP3 transcription factor. *Immunity* 30, 899–911. <https://doi.org/10.1016/j.immuni.2009.03.019>.
70. Wei, G., Wei, L., Zhu, J., Zang, C., Hu-Li, J., Yao, Z., Cui, K., Kanno, Y., Roh, T.Y., Watford, W.T., et al. (2009). Global mapping of H3K4me3 and H3K27me3 reveals specificity and plasticity in lineage fate determination of differentiating CD4+ T cells. *Immunity* 30, 155–167. <https://doi.org/10.1016/j.immuni.2008.12.009>.
71. Abbas, A.R., Wolslegel, K., Seshasayee, D., Modrusan, Z., and Clark, H.F. (2009). Deconvolution of blood microarray data identifies cellular activation patterns in systemic lupus erythematosus. *PLoS One* 4, e6098. <https://doi.org/10.1371/journal.pone.0006098>.
72. Zemmour, D., Zilionis, R., Kiner, E., Klein, A.M., Mathis, D., and Benoist, C. (2018). Single-cell gene expression reveals a landscape of regulatory T cell phenotypes shaped by the TCR. *Nat. Immunol.* 19, 291–301. <https://doi.org/10.1038/s41590-018-0051-0>.
73. Miragaia, R.J., Gomes, T., Chomka, A., Jardine, L., Riedel, A., Hegazy, A.N., Whibley, N., Tucci, A., Chen, X., Lindeman, I., et al. (2019). Single-cell transcriptomics of regulatory T cells reveals trajectories of tissue adaptation. *Immunity* 50, 493–504.e7. <https://doi.org/10.1016/j.immuni.2019.01.001>.
74. Hori, S., Haury, M., Coutinho, A., and Demengeot, J. (2002). Specificity requirements for selection and effector functions of CD25+4+ regulatory T cells in anti-myelin basic protein T cell receptor transgenic mice. *Proc. Natl. Acad. Sci. USA.* 99, 8213–8218. <https://doi.org/10.1073/pnas.122224799>.
75. Tarbell, K.V., Yamazaki, S., Olson, K., Toy, P., and Steinman, R.M. (2004). CD25+ CD4+ T cells, expanded with dendritic cells presenting a single autoantigenic peptide, suppress autoimmune diabetes. *J. Exp. Med.* 199, 1467–1477. <https://doi.org/10.1084/jem.20040180>.
76. Plitas, G., Konopacki, C., Wu, K., Bos, P.D., Morrow, M., Putintseva, E.V., Chudakov, D.M., and Rudensky, A.Y. (2016). Regulatory T cells exhibit distinct features in human breast cancer. *Immunity* 45, 1122–1134. <https://doi.org/10.1016/j.immuni.2016.10.032>.
77. Malchow, S., Leventhal, D.S., Nishi, S., Fischer, B.I., Shen, L., Paner, G.P., Amit, A.S., Kang, C., Geddes, J.E., Allison, J.P., et al. (2013). Aire-dependent thymic development of tumor-associated regulatory T cells. *Science* 339, 1219–1224. <https://doi.org/10.1126/science.1233913>.
78. Zheng, C., Zheng, L., Yoo, J.K., Guo, H., Zhang, Y., Guo, X., Kang, B., Hu, R., Huang, J.Y., Zhang, Q., et al. (2017). Landscape of infiltrating T cells in liver cancer revealed by single-cell sequencing. *Cell* 169, 1342–1356.e16. <https://doi.org/10.1016/j.cell.2017.05.035>.
79. Delgoffe, G.M., Woo, S.R., Turnis, M.E., Gravano, D.M., Guy, C., Overacre, A.E., Bettini, M.L., Vogel, P., Finkelstein, D., Bonnevier, J., et al. (2013). Stability and function of regulatory T cells is maintained by a neuropilin-1-semaphorin-4a axis. *Nature* 501, 252–256. <https://doi.org/10.1038/nature12428>.
80. Stagg, J., Divisekera, U., Duret, H., Sparwasser, T., Teng, M.W.L., Darcy, P.K., and Smyth, M.J. (2011). CD73-deficient mice have increased anti-tumor immunity and are resistant to experimental metastasis. *Cancer Res.* 71, 2892–2900. <https://doi.org/10.1158/0008-5472.CAN-10-4246>.
81. Shalev, I., Liu, H., Koscik, C., Bartczak, A., Javadi, M., Wong, K.M., Maknojia, A., He, W., Liu, M.F., Diao, J., et al. (2008). Targeted deletion of fgl2 leads to impaired regulatory T cell activity and development of autoimmune glomerulonephritis. *J. Immunol.* 180, 249–260. <https://doi.org/10.4049/jimmunol.180.1.249>.
82. Koch, M.A., Tucker-Heard, G., Perdue, N.R., Killebrew, J.R., Urdahl, K.B., and Campbell, D.J. (2009). The transcription factor T-bet controls regulatory T cell homeostasis and function during type 1 inflammation. *Nat. Immunol.* 10, 595–602. <https://doi.org/10.1038/ni.1731>.
83. Condino-Neto, A., and Newburger, P.E. (2000). Interferon-gamma improves splicing efficiency of CYBB gene transcripts in an interferon-responsive variant of chronic granulomatous disease due to a splice site consensus region mutation. *Blood* 95, 3548–3554.
84. You, M., Yu, D.H., and Feng, G.S. (1999). Shp-2 tyrosine phosphatase functions as a negative regulator of the interferon-stimulated Jak/STAT pathway. *Mol. Cell Biol.* 19, 2416–2424. <https://doi.org/10.1128/MCB.19.3.2416>.
85. Perkey, E., Maurice De Sousa, D., Carrington, L., Chung, J., Dils, A., Granadier, D., Koch, U., Radtke, F., Ludewig, B., Blazar, B.R., et al. (2020). GCNT1-mediated O-glycosylation of the sialomucin CD43 is a sensitive indicator of notch signaling in activated T cells. *J. Immunol.* 204, 1674–1688. <https://doi.org/10.4049/jimmunol.1901194>.
86. Hutloff, A., Dittrich, A.M., Beier, K.C., Eljaschewitsch, B., Kraft, R., Anagnostopoulos, I., and Kroczeck, R.A. (1999). ICOS is an inducible T-cell co-stimulator structurally and functionally related to CD28. *Nature* 397, 263–266. <https://doi.org/10.1038/16717>.
87. Kakugawa, K., Kojo, S., Tanaka, H., Seo, W., Endo, T.A., Kitagawa, Y., Muroi, S., Tenno, M., Yasmin, N., Kohwi, Y., et al. (2017). Essential roles of SATB1 in specifying T lymphocyte subsets. *Cell Rep.* 19, 1176–1188. <https://doi.org/10.1016/j.celrep.2017.04.038>.

88. Kashiwakura, Y., Sakurai, D., Kanno, Y., Hashiguchi, M., Kobayashi, A., Kurosu, A., Tokudome, S., Kobata, T., and Kojima, H. (2013). CD2-mediated regulation of peripheral CD4(+) CD25(+) regulatory T-cell apoptosis accompanied by down-regulation of Bim. *Immunology* 139, 48–60. <https://doi.org/10.1111/imm.12054>.
89. Li, A., Herbst, R.H., Canner, D., Schenkel, J.M., Smith, O.C., Kim, J.Y., Hillman, M., Bhutkar, A., Cuoco, M.S., Rappazzo, C.G., et al. (2019). IL-33 signaling alters regulatory T cell diversity in support of tumor development. *Cell Rep.* 29, 2998–3008.e8. <https://doi.org/10.1016/j.celrep.2019.10.120>.
90. Halim, L., Romano, M., McGregor, R., Correa, I., Pavlidis, P., Grageda, N., Hoong, S.J., Yuksel, M., Jassem, W., Hannen, R.F., et al. (2017). An atlas of human regulatory T helper-like cells reveals features of Th2-like tregs that support a tumorigenic environment. *Cell Rep.* 20, 757–770. <https://doi.org/10.1016/j.celrep.2017.06.079>.
91. Huang, S., Hendriks, W., Althage, A., Hemmi, S., Bluethmann, H., Kamijo, R., Vilcek, J., Zinkernagel, R.M., and Aguet, M. (1993). Immune response in mice that lack the interferon-gamma receptor. *Science* 259, 1742–1745. <https://doi.org/10.1126/science.8456301>.
92. Müller, U., Steinhoff, U., Reis, L.F., Hemmi, S., Pavlovic, J., Zinkernagel, R.M., and Aguet, M. (1994). Functional role of type I and type II interferons in antiviral defense. *Science* 264, 1918–1921. <https://doi.org/10.1126/science.8009221>.
93. Sade-Feldman, M., Yizhak, K., Bjorgaard, S.L., Ray, J.P., de Boer, C.G., Jenkins, R.W., Lieb, D.J., Chen, J.H., Frederick, D.T., Barzily-Rokni, M., et al. (2018). Defining T cell states associated with response to checkpoint immunotherapy in melanoma. *Cell* 175, 998–1013.e20. <https://doi.org/10.1016/j.cell.2018.10.038>.
94. Bradley, K.C., Finsterbusch, K., Schnepf, D., Crotta, S., Llorian, M., Davidson, S., Fuchs, S.Y., Staeheli, P., and Wack, A. (2019). Microbiota-driven tonic interferon signals in lung stromal cells protect from influenza virus infection. *Cell Rep.* 28, 245–256.e4. <https://doi.org/10.1016/j.celrep.2019.05.105>.
95. Maurice, N.J., McElrath, M.J., Andersen-Nissen, E., Frahm, N., and Prlic, M. (2019). CXCR3 enables recruitment and site-specific bystander activation of memory CD8(+) T cells. *Nat. Commun.* 10, 4987. <https://doi.org/10.1038/s41467-019-12980-2>.
96. Bangs, D.J., Tsitsiklis, A., Steier, Z., Chan, S.W., Kaminski, J., Streets, A., Yosef, N., and Robey, E.A. (2022). CXCR3 regulates stem and proliferative CD8+ T cells during chronic infection by promoting interactions with DCs in splenic bridging channels. *Cell Rep.* 38, 110266. <https://doi.org/10.1016/j.celrep.2021.110266>.
97. Groom, J.R., Richmond, J., Murooka, T.T., Sorensen, E.W., Sung, J.H., Bankert, K., von Andrian, U.H., Moon, J.J., Mempel, T.R., and Luster, A.D. (2012). CXCR3 chemokine receptor-ligand interactions in the lymph node optimize CD4+ T helper 1 cell differentiation. *Immunity* 37, 1091–1103. <https://doi.org/10.1016/j.immuni.2012.08.016>.
98. Rapp, M., Wintergerst, M.W.M., Kunz, W.G., Vetter, V.K., Knott, M.M.L., Lisowski, D., Haubner, S., Moder, S., Thaler, R., Eiber, S., et al. (2019). CCL22 controls immunity by promoting regulatory T cell communication with dendritic cells in lymph nodes. *J. Exp. Med.* 216, 1170–1181. <https://doi.org/10.1084/jem.20170277>.
99. Coghill, J.M., Fowler, K.A., West, M.L., Fulton, L.M., van Deventer, H., McKinnon, K.P., Vincent, B.G., Lin, K., Panoskaltsis-Mortari, A., Cook, D.N., et al. (2013). CC chemokine receptor 8 potentiates donor Treg survival and is critical for the prevention of murine graft-versus-host disease. *Blood* 122, 825–836. <https://doi.org/10.1182/blood-2012-06-435735>.
100. Muthuswamy, R., Urban, J., Lee, J.J., Reinhart, T.A., Bartlett, D., and Kalinski, P. (2008). Ability of mature dendritic cells to interact with regulatory T cells is imprinted during maturation. *Cancer Res.* 68, 5972–5978. <https://doi.org/10.1158/0008-5472.CAN-07-6818>.
101. Curtissinger, J.M., Agarwal, P., Lins, D.C., and Mescher, M.F. (2012). Autocrine IFN-gamma promotes naive CD8 T cell differentiation and synergizes with IFN-alpha to stimulate strong function. *J. Immunol.* 189, 659–668. <https://doi.org/10.4049/jimmunol.1102727>.
102. Tau, G.Z., Cowan, S.N., Weisburg, J., Braunstein, N.S., and Rothman, P.B. (2001). Regulation of IFN-gamma signaling is essential for the cytotoxic activity of CD8(+) T cells. *J. Immunol.* 167, 5574–5582. <https://doi.org/10.4049/jimmunol.167.10.5574>.
103. Bhat, P., Leggatt, G., Waterhouse, N., and Frazer, I.H. (2017). Interferon-gamma derived from cytotoxic lymphocytes directly enhances their motility and cytotoxicity. *Cell Death Dis.* 8, e2836. <https://doi.org/10.1038/cddis.2017.67>.
104. Horton, B.L., Fessenden, T.B., and Spranger, S. (2019). Tissue site and the cancer immunity cycle. *Trends Cancer* 5, 593–603. <https://doi.org/10.1016/j.trecan.2019.07.006>.
105. Zagorulya, M., Duong, E., and Spranger, S. (2020). Impact of anatomic site on antigen-presenting cells in cancer. *J. Immunother. Cancer* 8, e001204. <https://doi.org/10.1136/jitc-2020-001204>.
106. Tan, T.G., Mathis, D., and Benoist, C. (2016). Singular role for T-BET+CXCR3+ regulatory T cells in protection from autoimmune diabetes. *Proc. Natl. Acad. Sci. USA* 113, 14103–14108. <https://doi.org/10.1073/pnas.1616710113>.
107. Choi, J., Ziga, E.D., Ritchey, J., Collins, L., Prior, J.L., Cooper, M.L., Piwnica-Worms, D., and DiPersio, J.F. (2012). IFNgammaR signaling mediates alloreactive T-cell trafficking and GVHD. *Blood* 120, 4093–4103. <https://doi.org/10.1182/blood-2012-01-403196>.
108. Levine, A.G., Mendoza, A., Hemmers, S., Molledo, B., Niec, R.E., Schizas, M., Hoyos, B.E., Putintseva, E.V., Chaudhry, A., Dikiy, S., et al. (2017). Stability and function of regulatory T cells expressing the transcription factor T-bet. *Nature* 546, 421–425. <https://doi.org/10.1038/nature22360>.
109. Lee, J.C., Mehdizadeh, S., Smith, J., Young, A., Mufazalov, I.A., Mowery, C.T., Daud, A., and Bluestone, J.A. (2020). Regulatory T cell control of systemic immunity and immunotherapy response in liver metastasis. *Sci. Immunol.* 5, eaba0759. <https://doi.org/10.1126/sciimmunol.aba0759>.
110. Huffnagle, G.B., Dickson, R.P., and Lukacs, N.W. (2017). The respiratory tract microbiome and lung inflammation: a two-way street. *Mucosal Immunol.* 10, 299–306. <https://doi.org/10.1038/mi.2016.108>.
111. Ramírez-Laborda, A.G., Isla, D., Artal, A., Arias, M., Rezusta, A., Pardo, J., and Gálvez, E.M. (2020). The influence of lung microbiota on lung carcinogenesis, immunity, and immunotherapy. *Trends Cancer* 6, 86–97. <https://doi.org/10.1016/j.trecan.2019.12.007>.
112. Lee, N., and Kim, W.U. (2017). Microbiota in T-cell homeostasis and inflammatory diseases. *Exp. Mol. Med.* 49, e340. <https://doi.org/10.1038/emm.2017.36>.
113. Ansaldi, E., Farley, T.K., and Belkaid, Y. (2021). Control of immunity by the microbiota. *Annu. Rev. Immunol.* 39, 449–479. <https://doi.org/10.1146/annurev-immunol-093019-112348>.
114. Tastan, C., Karhan, E., Zhou, W., Fleming, E., Voigt, A.Y., Yao, X., Wang, L., Horne, M., Placek, L., Kozhaya, L., et al. (2018). Tuning of human MAIT cell activation by commensal bacteria species and MR1-dependent T-cell presentation. *Mucosal Immunol.* 11, 1591–1605. <https://doi.org/10.1038/s41385-018-0072-x>.
115. Ataide, M.A., Knöpper, K., Cruz de Casas, P., Ugur, M., Eickhoff, S., Zou, M., Shaikh, H., Trivedi, A., Grafen, A., Yang, T., et al. (2022). Lymphatic migration of unconventional T cells promotes site-specific immunity in distinct lymph nodes. *Immunity* 55, 1813–1828.e9. <https://doi.org/10.1016/j.jimmuni.2022.07.019>.
116. Sullivan, M.R., Danai, L.V., Lewis, C.A., Chan, S.H., Gui, D.Y., Kunchok, T., Dennstedt, E.A., Vander Heiden, M.G., and Muir, A. (2019). Quantification of microenvironmental metabolites in murine cancers reveals determinants of tumor nutrient availability. *Elife* 8, e44235. <https://doi.org/10.7554/elife.44235>.
117. Feng, Q., Liu, Z., Yu, X., Huang, T., Chen, J., Wang, J., Wilhelm, J., Li, S., Song, J., Li, W., et al. (2022). Lactate increases stemness of CD8 + T cells to augment anti-tumor immunity. *Nat. Commun.* 13, 4981. <https://doi.org/10.1038/s41467-022-32521-8>.

118. Best, S.A., Gubser, P.M., Sethumadhavan, S., Kersbergen, A., Negrón Abril, Y.L., Goldford, J., Sellers, K., Abeysekera, W., Garnham, A.L., McDonald, J.A., et al. (2022). Glutaminase inhibition impairs CD8 T cell activation in STK11/Lkb1-deficient lung cancer. *Cell Metab.* 34, 874–887.e6. <https://doi.org/10.1016/j.cmet.2022.04.003>.
119. Zhao, S., Peralta, R.M., Avina-Ochoa, N., Delgoffe, G.M., and Kaech, S.M. (2021). Metabolic regulation of T cells in the tumor microenvironment by nutrient availability and diet. *Semin. Immunol.* 52, 101485. <https://doi.org/10.1016/j.smim.2021.101485>.
120. Peng, X., He, Y., Huang, J., Tao, Y., and Liu, S. (2021). Metabolism of dendritic cells in tumor microenvironment: for immunotherapy. *Front. Immunol.* 12, 613492. <https://doi.org/10.3389/fimmu.2021.613492>.
121. Watson, M.J., Vignali, P.D.A., Mullett, S.J., Overacre-Delgoffe, A.E., Peralta, R.M., Grebinoski, S., Menk, A.V., Rittenhouse, N.L., DePeaux, K., Whetstone, R.D., et al. (2021). Metabolic support of tumour-infiltrating regulatory T cells by lactic acid. *Nature* 591, 645–651. <https://doi.org/10.1038/s41586-020-03045-2>.
122. Nüssing, S., Trapani, J.A., and Parish, I.A. (2020). Revisiting T cell tolerance as a checkpoint target for cancer immunotherapy. *Front. Immunol.* 11, 589641. <https://doi.org/10.3389/fimmu.2020.589641>.
123. Wohn, C., Le Guen, V., Voluzan, O., Fiore, F., Henri, S., and Malissen, B. (2020). Absence of MHC class II on cDC1 dendritic cells triggers fatal autoimmunity to a cross-presented self-antigen. *Sci. Immunol.* 5, eaba1896. <https://doi.org/10.1126/sciimmunol.aba1896>.
124. Ruhland, M.K., Roberts, E.W., Cai, E., Mujal, A.M., Marchuk, K., Beppler, C., Nam, D., Serwas, N.K., Binnewies, M., and Krummel, M.F. (2020). Visualizing synaptic transfer of tumor antigens among dendritic cells. *Cancer Cell* 37, 786–799.e5. <https://doi.org/10.1016/j.ccr.2020.05.002>.
125. de Mingo Pulido, Á., Gardner, A., Hiebler, S., Soliman, H., Rugo, H.S., Krummel, M.F., Coussens, L.M., and Ruffell, B. (2018). TIM-3 regulates CD103(+) dendritic cell function and response to chemotherapy in breast cancer. *Cancer Cell* 33, 60–74.e6. <https://doi.org/10.1016/j.ccr.2017.11.019>.
126. Gerner, M.Y., Kastenmuller, W., Ifrim, I., Kabat, J., and Germain, R.N. (2012). Histo-cytometry: a method for highly multiplex quantitative tissue imaging analysis applied to dendritic cell subset microanatomy in lymph nodes. *Immunity* 37, 364–376. <https://doi.org/10.1016/j.immuni.2012.07.011>.
127. Momin, N., Mehta, N.K., Bennett, N.R., Ma, L., Palmeri, J.R., Chinn, M.M., Lutz, E.A., Kang, B., Irvine, D.J., Spranger, S., and Wittrup, K.D. (2019). Anchoring of intratumorally administered cytokines to collagen safely potentiates systemic cancer immunotherapy. *Sci. Transl. Med.* 11, eaaw2614. <https://doi.org/10.1126/scitranslmed.aaw2614>.
128. Zhu, E.F., Gai, S.A., Opel, C.F., Kwan, B.H., Surana, R., Mihm, M.C., Kauke, M.J., Moynihan, K.D., Angelini, A., Williams, R.T., et al. (2015). Synergistic innate and adaptive immune response to combination immunotherapy with anti-tumor antigen antibodies and extended serum half-life IL-2. *Cancer Cell* 27, 489–501. <https://doi.org/10.1016/j.ccr.2015.03.004>.
129. Hughes, T.K., Wadsworth, M.H., 2nd, Gierahn, T.M., Do, T., Weiss, D., Andrade, P.R., Ma, F., de Andrade Silva, B.J., Shao, S., Tsui, L.C., et al. (2020). Second-strand synthesis-based massively parallel scRNA-seq reveals cellular states and molecular features of human inflammatory skin pathologies. *Immunity* 53, 878–894.e7. <https://doi.org/10.1016/j.immuni.2020.09.015>.
130. Gierahn, T.M., Wadsworth, M.H., 2nd, Hughes, T.K., Bryson, B.D., Butler, A., Satija, R., Fortune, S., Love, J.C., and Shalek, A.K. (2017). Seq-Well: portable, low-cost RNA sequencing of single cells at high throughput. *Nat. Methods* 14, 395–398. <https://doi.org/10.1038/nmeth.4179>.
131. Stoeckius, M., Zheng, S., Houck-Loomis, B., Hao, S., Yeung, B.Z., Mauck, W.M., 3rd, Smibert, P., and Satija, R. (2018). Cell Hashing with barcoded antibodies enables multiplexing and doublet detection for single cell genomics. *Genome Biol.* 19, 224. <https://doi.org/10.1186/s13059-018-1603-1>.
132. Roelli, P., Flynn, B., and Gui, G. (2019). Hoohm/CITE-seq-Count: 1.4.2 (Zenodo). <https://doi.org/10.5281/zenodo.2590196> Version 1.4.2..
133. Macosko, E.Z., Basu, A., Satija, R., Nemesh, J., Shekhar, K., Goldman, M., Tirosh, I., Bialas, A.R., Kamitaki, N., Martersteck, E.M., et al. (2015). Highly parallel genome-wide expression profiling of individual cells using nanoliter droplets. *Cell* 161, 1202–1214. <https://doi.org/10.1016/j.cell.2015.05.002>.
134. Hafemeister, C., and Satija, R. (2019). Normalization and variance stabilization of single-cell RNA-seq data using regularized negative binomial regression. *Genome Biol.* 20, 296. <https://doi.org/10.1186/s13059-019-1874-1>.
135. Butler, A., Hoffman, P., Smibert, P., Papalexi, E., and Satija, R. (2018). Integrating single-cell transcriptomic data across different conditions, technologies, and species. *Nat. Biotechnol.* 36, 411–420. <https://doi.org/10.1038/nbt.4096>.
136. Liberzon, A., Subramanian, A., Pinchback, R., Thorvaldsdóttir, H., Tamayo, P., and Mesirov, J.P. (2011). Molecular signatures database (MSigDB) 3.0. *Bioinformatics* 27, 1739–1740. <https://doi.org/10.1093/bioinformatics/btr260>.
137. Tu, A.A., Gierahn, T.M., Monian, B., Morgan, D.M., Mehta, N.K., Ruiter, B., Shreffler, W.G., Shalek, A.K., and Love, J.C. (2019). TCR sequencing paired with massively parallel 3' RNA-seq reveals clonotypic T cell signatures. *Nat. Immunol.* 20, 1692–1699. <https://doi.org/10.1038/s41590-019-0544-5>.
138. Vander Heiden, J.A., Yaari, G., Uzman, M., Stern, J.N.H., O'Connor, K.C., Hafler, D.A., Vigneault, F., and Kleinstein, S.H. (2014). pRESTO: a toolkit for processing high-throughput sequencing raw reads of lymphocyte receptor repertoires. *Bioinformatics* 30, 1930–1932. <https://doi.org/10.1093/bioinformatics/btu138>.
139. Gupta, N.T., Vander Heiden, J.A., Uzman, M., Gadala-Maria, D., Yaari, G., and Kleinstein, S.H. (2015). Change-O: a toolkit for analyzing large-scale B cell immunoglobulin repertoire sequencing data. *Bioinformatics* 31, 3356–3358. <https://doi.org/10.1093/bioinformatics/btv359>.
140. Smith, T., Heger, A., and Sudbery, I. (2017). UMI-tools: modelling sequencing errors in unique molecular identifiers to improve quantification accuracy. *Genome Res.* 27, 491–499. <https://doi.org/10.1101/gr.209601.116>.
141. Burger, M.L., Cruz, A.M., Crossland, G.E., Gaglia, G., Ritch, C.C., Blatt, S.E., Bhutkar, A., Canner, D., Kienka, T., Tavana, S.Z., et al. (2021). Antigen dominance hierarchies shape TCF1(+) progenitor CD8 T cell phenotypes in tumors. *Cell* 184, 4996–5014.e26. <https://doi.org/10.1016/j.cell.2021.08.020>.
142. Liberzon, A., Birger, C., Thorvaldsdóttir, H., Ghandi, M., Mesirov, J.P., and Tamayo, P. (2015). The Molecular Signatures Database (MSigDB) hallmark gene set collection. *Cell Syst.* 1, 417–425. <https://doi.org/10.1016/j.cels.2015.12.004>.
143. Skinner, J. (2018). Statistics for immunologists. *Curr. Protoc. Immunol.* 122, 54. <https://doi.org/10.1002/cpim.54>.

STAR★METHODS

KEY RESOURCES TABLE

REAGENT or RESOURCE	SOURCE	IDENTIFIER
Antibodies		
anti-GFP chicken; polyclonal	abcam	Cat# ab13970; AB_300798
anti-mouse CD103 (APC); clone 2E7	eBioscience	Cat# 17-1031-82; AB_1106992
anti-mouse CD11c (BUV496); clone N418	BD Biosciences	Cat# 750450; AB_2874611
anti-mouse CD11c (BV421); clone N418	BioLegend	Cat# 117330; AB_11219593
anti-mouse CD11c (BV605); clone N418	BioLegend	Cat# 117334; AB_2562415
anti-mouse CD152 (CTLA-4) (PE-CF594); clone UC10-4F10-11	BD Biosciences	Cat# 564332; AB_2732917
anti-mouse CD16/32; clone 93	BioLegend	Cat# 101330; AB_2561482
anti-mouse CD183 (CXCR3) (PE); clone CXCR3-173	BioLegend	Cat# 126505; AB_1027656
anti-mouse CD183 (CXCR3) (PE/Dazzle 594); clone CXCR3-173	BioLegend	Cat# 126534; AB_2566563
anti-mouse CD19 (APC-Cy7); clone 6D5	BioLegend	Cat# 115530; AB_830707
anti-mouse CD19 (BV605); clone 6D5	BioLegend	Cat# 115540; AB_2563067
anti-mouse CD19 (PE); clone 1D3/CD19	BioLegend	Cat# 152408; AB_2629817
anti-mouse CD197 (CCR7) (BV786); clone 4B12	BD Biosciences	Cat# 564355; AB_2738765
anti-mouse CD25 (BUV395); clone PC61	BD Biosciences	Cat# 564022; AB_2722574
anti-mouse CD25 (APC-Cy7); clone PC61	BioLegend	Cat# 102025; AB_830744
anti-mouse CD25 (FITC); clone PC61	BioLegend	Cat# 102005; AB_312854
anti-mouse CD25 (BV421); clone PC61	BioLegend	Cat# 102034; AB_11203373
anti-mouse CD274 (PD-L1) (BV605); clone 10F.9G2	BioLegend	Cat# 124321; AB_2563635
anti-mouse CD279 (PD-1) (PE-Cy7); clone RMP1-30	BioLegend	Cat# 109110; AB_572017
anti-mouse CD28; clone 37.51	BD Biosciences	Cat# 553294; AB_394763
anti-mouse CD28; clone 37.51	Bio X Cell	Cat# BE0015-1; AB_1107624
anti-mouse CD304 (Neuropilin-1) (BV421); clone _3E12	BioLegend	Cat# 145209; AB_2562358
anti-mouse CD366 (TIM3) (PE-Cy7); clone RMT3-23	eBioscience	Cat# 25-5870-82; AB_2573483
anti-mouse CD39 (PE-Cy7); clone 24DMS1	eBioscience	Cat# 25-0391-82; AB_1210766
anti-mouse CD3e (BUV496); clone 145-2C11	BD Biosciences	Cat# 612955; AB_2870231
anti-mouse CD3e (BUV661); clone 17A2	BD Biosciences	Cat# 741562; AB_2870988
anti-mouse CD3e; clone 145-2C11	BD Biosciences	Cat# 553057; AB_394590
anti-mouse CD3e (APC-Cy7); clone 17A2	BioLegend	Cat# 100222; AB_2242784
anti-mouse CD3e (BV711); clone 17A2	BioLegend	Cat# 100241; AB_2563945
anti-mouse CD3e (PE); clone 17A2	BioLegend	Cat# 100206; AB_312663
anti-mouse CD3e (eFluor450); clone 17A2	eBioscience	Cat# 48-0032-80; AB_1272229
anti-mouse CD3e (APC); clone 145-2C11	eBioscience	Cat# 17-0031-82; AB_469315
anti-mouse CD3e (BV605); clone 145-2C11	BioLegend	Cat# 100351; AB_2565842
anti-mouse CD4 (BUV737); clone RM4-5	BD Biosciences	Cat# 564933; AB_2732918
anti-mouse CD4 (PerCP-Cy5.5); clone RM4-5	BioLegend	Cat# 100540; AB_893326
anti-mouse CD4 (BV650); clone RM4-5	BioLegend	Cat# 100555; AB_2562529
anti-mouse CD40 (BV711); clone 3/23	BD Biosciences	Cat# 740700; AB_2740384
anti-mouse CD44 (BV480); clone IM7	BD Biosciences	Cat# 566116; AB_2739518
anti-mouse CD45 (BUV395); clone 30-F11	BD Biosciences	Cat# 564279; AB_2651134
anti-mouse CD45 (BV786); clone 30-F11	BD Biosciences	Cat# 564225; AB_2716861
anti-mouse CD45 (APC); clone 30-F11	BioLegend	Cat# 103112; AB_312977
anti-mouse CD45 (PE-Cy7); clone 30-F11	BioLegend	Cat# 103113; AB_312978
anti-mouse CD45 (PE); clone 30-F11	BioLegend	Cat# 103105; AB_312970

(Continued on next page)

Continued

REAGENT or RESOURCE	SOURCE	IDENTIFIER
anti-mouse CD45 (BUV563); clone 30-F11	BD Biosciences	Cat# 612924; AB_2870209
anti-mouse CD45.1 (BUV395); clone A20	BD Biosciences	Cat# 565212; AB_2722493
anti-mouse CD45.1 (BV650); clone A20	BioLegend	Cat# 110736; AB_2562564
anti-mouse CD45.1 (APC); clone A20	BioLegend	Cat# 110713; AB_313502
anti-mouse CD45.2 (BUV395); clone 104	BD Biosciences	Cat# 564616; AB_2738867
anti-mouse CD45.2 (BUV563); clone 104	BD Biosciences	Cat# 741273; AB_2870814
anti-mouse CD45.2 (PE); clone 104	BioLegend	Cat# 109807; AB_313444
anti-mouse CD62L (BV650); clone MEL-14	BioLegend	Cat# 104453; AB_2800559
anti-mouse CD73 (PerCP-eFluor710); clone eBioTY/11.8	eBioscience	Cat# 46-0731-80; AB_10854727
anti-mouse CD80 (PE-Cy7); clone 16-10A1	BioLegend	Cat# 104733; AB_2563112
anti-mouse CD86 (AF700); clone PO3	BioLegend	Cat# 105122; AB_493723
anti-mouse CD8a (BUV395); clone 53-6.7	BD Biosciences	Cat# 563786; AB_2732919
anti-mouse CD8a (BUV737); clone 53-6.7	BD Biosciences	Cat# 564297; AB_2722580
anti-mouse CD8a (BUV805); clone 53-6.7	BD Biosciences	Cat# 612898; AB_2870186
anti-mouse CD8a (PE-CF594); clone 53-6.7	BD Biosciences	Cat# 562315; AB_11154579
anti-mouse CD8a (BV605); clone 53-6.7	BioLegend	Cat# 100744; AB_2562609
anti-mouse CD8a (BV711); clone 53-6.7	BioLegend	Cat# 100759; AB_2563510
anti-mouse F4/80 (PE-Cy7); clone BM8	BioLegend	Cat# 123113; AB_893490
anti-mouse F4/80 (BV785); clone BM8	BioLegend	Cat# 123141; AB_2563667
anti-mouse F4/80 (BV650); clone BM8	BioLegend	Cat# 123149; AB_2564589
anti-mouse FoxP3 (PerCP-Cy5.5); clone FJK-16s	eBioscience	Cat# 45-5773-80; AB_914349
anti-mouse FoxP3 (PE-Cy5); clone FJK-16s	eBioscience	Cat# 15-5773-82; AB_468806
anti-mouse GATA3 (BUV395); clone L50-823	BD Biosciences	Cat# 565448; AB_2739241
anti-mouse IFNg; clone XMG1.2	Bio X Cell	Cat# BE0055; AB_1107694
anti-mouse IL-12/IL-23 p40 (PE); clone C17.8	eBioscience	Cat# 12-7123-82; AB_466185
anti-mouse Ki-67 (BV711); clone B56	BD Biosciences	Cat# 563755; AB_2738406
anti-mouse LAP (TGF- β 1) (PE); clone TW7-16B4	BioLegend	Cat# 141305; AB_10717505
anti-mouse Ly-6C (PE); clone HK1.4	BioLegend	Cat# 128007; AB_1186133
anti-mouse Ly-6C (eFluor450); clone HK1.4	eBioscience	Cat# 48-5932-80; AB_10805518
anti-mouse MHC-II (I-A/I-E) (BUV805); clone M5/114.15.2	BD Biosciences	Cat# 748844; AB_2873247
anti-mouse MHC-II (I-A/I-E) (–); clone M5/114	Bio X Cell	Cat# BE0108; AB_10949298
anti-mouse MHC-II (I-A/I-E) (BV510); clone M5/114.15.2	BioLegend	Cat# 107636; AB_2734168
anti-mouse MHC-II (I-A/I-E) (AF700); clone M5/114.15.2	eBioscience	Cat# 56-5321-80; AB_494010
anti-mouse NK1.1 (APC-Cy7); clone PK136	BioLegend	Cat# 108724; AB_830871
anti-mouse NK1.1 (BV711); clone PK136	BioLegend	Cat# 108745; AB_2563286
anti-mouse ROR γ t (BV786); clone Q31-378	BD Biosciences	Cat# 564723; AB_2738916
anti-mouse Thy1.1 (BUV496); clone HIS51	BD Biosciences	Cat# 741109; AB_2870701
anti-mouse Thy1.2 (PE-Cy7); clone 53-2.1	BioLegend	Cat# 140310; AB_10643586
anti-mouse/human CD11b (PE/Dazzle 594); clone M1/70	BioLegend	Cat# 101256; AB_2563648
anti-mouse/human FoxP3 (AF750); clone 1054C	R&D Systems	Cat# IC8214S
anti-mouse/human Gzmb (AF700); clone QA16A02	BioLegend	Cat# 372221; AB_2728388
anti-mouse/human Helios (PE); clone 22F6	BioLegend	Cat# 137206; AB_10552903
anti-mouse/human T-bet (BV785); clone 4B10	BioLegend	Cat# 644835; AB_2721566
anti-mouse/human T-bet (BV711); clone 4B10	BioLegend	Cat# 644820; AB_2715766
anti-mouse/human TCF1 (AF488); clone C63D9	Cell Signaling Technology	Cat# 6444S

(Continued on next page)

Continued

REAGENT or RESOURCE	SOURCE	IDENTIFIER
recombinant human Flt3L-Ig; clone Flt-3L-Ig (hum./hum.)	Bio X Cell	Cat# BE0098; AB_10949072
Chemicals, peptides, and recombinant proteins		
Fixable Viability Dye eFluor780	eBioscience	Cat# 65-0865-18
Fixable Viability Dye eFluor506	eBioscience	Cat# 65-0863-18
Fixable Viability Dye eFluor450	eBioscience	Cat# 65-0866-14
Brefeldin A Solution	BioLegend	Cat# 420601
Streptavidin-PE	Invitrogen	Cat# S21388
H-2K(b) chicken ova 257–264 SIINFEKL	NIH Tetramer Core Facility	N/A
Biotinylated Monomer		
Liberase TL Research Grade	Sigma-Aldrich	Cat# 05401020001
DNase I, Grade II, from bovine pancreas	Sigma-Aldrich	Cat# 10104159001
Diphtheria Toxin from Corynebacterium	Sigma-Aldrich	Cat# D0564
SIINFEKL peptide (OVA257–264)	Invivogen	Cat# vac-sin
Phorbol 12-myristate 13-acetate	Sigma-Aldrich	Cat# P8139
Ionomycin from Streptomyces conglobatus	Sigma-Aldrich	Cat# I9657
Poly(I:C) HMW	Invivogen	Cat# tirl-pic
Recombinant rmouse GM-CSF	BioLegend	Cat# 576304
Recombinant mouse IL-12 protein fused to murine serum albumin (IL-12-MSA)	Dane Wittrup Lab (MIT)	N/A
cOmplete Protease Inhibitor Cocktail	Sigma-Aldrich	Cat# 11697498001
T-PER Tissue Protein Extraction Reagent	Thermo Scientific	Cat# 78510
Critical commercial assays		
Mouse IFNg ELISpot Kit	BD Biosciences	Cat# 551083
AEC Substrate Set	BD Biosciences	Cat# 551951
Mouse IFN-gamma DuoSet ELISA	R&D Systems	Cat# DY485-05
Mouse IL-2 DuoSet ELISA	R&D Systems	Cat# DY402-05
CellTrace Violet Cell Proliferation Kit	Invitrogen	Cat# C34571
Precision Count Beads	BioLegend	Cat# 424902
UltraComp eBeads Compensation Beads	Invitrogen	Cat# 01-2222-42
FoxP3 Transcription Factor Staining Buffer Set	eBioscience	Cat# 00-5523-00
Cytofix/Cytoperm Fixation/Permeabilization Buffer Set	BD Cytofix/Cytoperm	Cat# 554714
In-Fusion HD Cloning Plus	Takara Bio	Cat# 639645
Mouse CD8a+ T cell Isolation Kit	Miltenyi Biotec	Cat# 130-104-075
Anti-PE MicroBeads	Miltenyi Biotec	Cat# 130-048-801
Mouse CD90.2 MicroBeads	Miltenyi Biotec	Cat# 130-121-278
Pro-Long Diamond Antifade Mountant	Invitrogen	Cat# P36961
Deposited data		
Murine scRNA-seq (ZsG ⁺ DC1:OT-I T cell and ZsG ⁺ DC1:Treg:OT-I T cell ex vivo co-cultures)	This paper	GSE216086
Murine scRNA-seq (CD45 ⁺ , CD3e ⁺ , CD8 ⁻ , CD4 ⁺ and CD25 ^{high} cells from KP-zSIIN tumor-draining and naive mLN and iLN)	This paper	GSE216086
Murine TCR-seq (CD45 ⁺ , CD3e ⁺ , CD8 ⁻ , CD4 ⁺ and CD25 ^{high} cells from KP-zSIIN tumor-draining and naive mLN and iLN)	This paper	GSE216086
Experimental models: Cell lines		
KP-zSIIN	This paper	N/A
KP-SIY	This paper	N/A

(Continued on next page)

Continued

REAGENT or RESOURCE	SOURCE	IDENTIFIER
Experimental models: Organisms/strains		
Mouse: C57BL/6	Jackson Laboratory	Strain# 000664
Mouse: C57BL/6	Taconic Biosciences	Strain# B6-F
Mouse: <i>Batf3</i> ^{-/-}	Jackson Laboratory	Strain# 013755
Mouse: <i>CD45.1</i> ⁺	Jackson Laboratory	Strain# 002014
Mouse: <i>Cxcr3</i> ^{-/-}	Jackson Laboratory	Strain# 005796
Mouse: <i>FoxP3</i> ^{DTR,eGFP}	Jackson Laboratory	Strain# 016958
Mouse: <i>H2-Ab1</i> ^{-/-}	Taconic Biosciences	Strain# ABBN12-F
Mouse: <i>Ifnar1</i> ^{-/-}	Jackson Laboratory	Strain# 028288
Mouse: <i>Ifngr1</i> ^{-/-}	Jackson Laboratory	Strain# 003288
Mouse: <i>Ifngr1</i> ^{-/-} <i>Ifnar1</i> ^{-/-}	Jackson Laboratory	Strain# 029098
Mouse: <i>p40-IRES-eYFP</i>	Jackson Laboratory	Strain# 006412
Mouse: OT-I TCR-transgenic	Jackson Laboratory	Strain# 003831
Mouse: <i>Rag2</i> ^{-/-}	Taconic Biosciences	Strain# RAGN12-F
Mouse: <i>Thy1.1</i> ⁺	Jackson Laboratory	Strain# 000406
Mouse: <i>XCR1</i> ^{DTR.Venus}	Riken	Strain# RBRC09485
Recombinant DNA		
Plasmid: pLV-EF1 α -IRES-puro vector	Addgene	Cat# 85132
Software and algorithms		
FlowJo v10.8.1	TreeStar	https://www.flowjo.com
GraphPad Prism v9	GraphPad	https://www.graphpad.com
Adobe Illustrator CC2023	Adobe	https://www.adobe.com
TissueFAXS Viewer v7.1	TissueGnostics USA	https://tissuegnostics.com/products/scanning-and-viewing-software/tissuefaxis-viewer
Imaris software v9.7.2	Bitplane	https://imaris.oxinst.com/
Seurat v2.3.4 and v3.0.0	Rahul Satija Lab (NYU)	https://www.satijalab.org/seurat/

RESOURCE AVAILABILITY**Lead contact**

Further information and requests for resources and reagents should be directed to and will be fulfilled by the lead contact, Stefani Spranger (spranger@mit.edu).

Materials availability

This study did not generate new unique reagents.

Data and code availability

The scRNA-seq data generated in this study has been deposited to the GEO database (GSE216086), and code used to process and analyze scRNA-seq data was made available at https://github.com/duncannmorgan/kptumors_immetry and is archived at <https://doi.org/10.5281/zenodo.7331914>. Code used for the spatial analysis of IF images was made available at <https://github.com/awedwards/DC-Treg-CD8T-interactions-project>. Any additional information required to reanalyze the data reported in this paper is available from the [lead contact](#) upon request.

EXPERIMENTAL MODEL AND SUBJECT DETAILS**Mice**

C57BL/6 mice were purchased from Taconic Biosciences or Jackson Laboratories. *H2-Ab1*^{-/-} mice were purchased from Taconic Biosciences. *Batf3*^{-/-}, *FoxP3*^{DTR,eGFP}, *p40-IRES-eYFP*, *Ifnar1*^{-/-}, *Ifngr1*^{-/-}, *Ifnar1*^{-/-}, *Cxcr3*^{-/-}, *Thy1.1*⁺ and *CD45.1*⁺ mice were purchased from Jackson Laboratories and bred in-house. TCR-transgenic OT-I *Rag2*^{-/-} and *XCR1*^{DTR.Venus} mice were bred and maintained in-house. All mice were housed under specific pathogen free conditions at the Koch Institute animal facility. Mice

were gender-matched and age-matched to be 6–12 weeks old at the time of experimentation. All experimental animal procedures were approved by the Committee on Animal Care at MIT.

Cell lines and tumor injections

KP-zSIIN and KP-SIY were cultured at 37°C and 5% CO₂ in DMEM (GIBCO) supplemented with 10% FBS (Atlanta Biologicals), 1% penicillin/streptomycin (GIBCO), and 1X non-essential amino acids (GIBCO). For tumor implantation, tumor cells were harvested by trypsinization (GIBCO), washed twice with 1X PBS (GIBCO), resuspended in PBS and 2.5x10⁵ tumor cells were injected subcutaneously or intravenously.

METHOD DETAILS

Generation of expression vectors and modified tumor cell lines

The pLV-EF1 α -IRES-puro vector (Addgene no. 85132) was linearized by digestion with BamHI and EcoRI restriction enzymes (NEB). The ZsGreen-SIINFEKL insert was generated using the pCAGGS_ZsGreen_minOVA construct (a gift from Max Krummel at UCSF), then cloned into the linearized pLV-EF1 α -IRES-puro vector using the In-Fusion cloning kit (Takara Bio). The resulting pLV-EF1 α -ZsGreen-SIINFEKL-IRES-puro construct was amplified and sequenced for accuracy. The KP-zSIIN cell line was genetically engineered to stably express ZsGreen-SIINFEKL using lentiviral transduction of the KP parental tumor line (a gift from Tyler Jacks) with the pLV-EF1a-cerulean-SIIN-SIY-IRES-puro construct. KP-zSIIN cell line was puromycin (GIBCO) selected and further FACS-sorted to enrich for cells with maximal expression of ZsGreen. Generation of the KP-SIY cell line was previously described.²⁴

Adoptive transfer of T cells

The *in vivo* priming assay was adapted from Horton et al.²⁴ Briefly, OT-I T cells were isolated from spleens and LN of *OT-I Rag2*^{-/-}CD45.1⁺ mice, labeled with CTV dye (Invitrogen) following manufacturer's instructions and at least 10⁶ (for flow analysis) or precisely 2.5x10⁴ cells (for immunostaining) were transferred retro-orbitally (*r.o.*) to mice with KP-zSIIN tumors at day 7 post-tumor implantation. Transferred OT-I T cells were analyzed in tDLN of recipient mice 3 days later. Frequency of proliferated T cells was quantified as the percentage of cells that had undergone one or more rounds of division, gated using an unstimulated, CTV-labeled sample as the undivided reference control. The T cell proliferation index was quantified as the total number of divisions divided by the number of cells that went into division using the proliferation modeling function in FlowJo v10.5.3 software (TreeStar).

Tissue processing for flow cytometry, cell sorting and ELISpot

LN were either directly mashed through a 70 μ m filter into RPMI (GIBCO) for T cell analysis, or processed using a method adapted from Ruhland et al.¹²⁴ for DC analysis and sorting. For the latter, LN were pierced with sharp forceps, incubated for 15 min at 37°C in digestion buffer (250 μ g/mL Liberase (Sigma-Aldrich) and 50 μ g/mL DNase (Sigma-Aldrich) in RPMI (GIBCO)), then pipetted up and down vigorously, followed by a second 15 min incubation at 37°C. The LN cell mixture was filtered through a 70 μ m filter to generate a single cell suspension. For sorting, LN cells were next incubated with α CD16/CD32 (clone 93, BioLegend) in FACS buffer (PBS (GIBCO) with 1% FBS (Atlanta Biologicals) and 2 mM EDTA (Invitrogen)) for 15 min at 4°C to prevent non-specific antibody binding, then washed with FACS buffer. The cells were then incubated with PE-labeled antibodies (α CD19-PE clone 1D3 and α CD3e-PE clone 17A2 if only DC were sorted, or α CD19-PE alone if Treg cells were also sorted, Biolegend) in FACS buffer for 10 min at 4°C, followed by negative selection using anti-PE microbeads (Miltenyi Biotec) according to manufacturer's instructions, prior to staining for FACS. Lungs and flank tumors were dissected, minced, then incubated in digestion buffer for 40 min at 37°C and mashed through a 70 μ m filter to generate a single cell suspension. Spleens were dissected and directly mashed through a 70 μ m filter to generate a single cell suspension. ACK Lysing Buffer (GIBCO) was used to lyse red blood cells in lungs and spleens (lysis performed for 2 min on ice, followed by two washes with PBS), prior to staining for flow or plating for ELISpot.

Flow cytometry and FACS staining

Cells were resuspended in FACS buffer (PBS (GIBCO) with 1% FBS (Atlanta Biologicals) and 2 mM EDTA (Invitrogen)) containing Fixable Viability Dye eFluor 780, eFluor 506 or eFluor 405 (eBioscience) to distinguish live and dead cells and α CD16/CD32 (clone 93, BioLegend) to prevent non-specific antibody binding, and incubated for 15 min at 4°C. Cells were then washed with FACS buffer and stained for surface proteins using fluorophore-conjugated antibodies resuspended in FACS buffer at the specified dilutions (Table S5) for 20 min at 4°C. Following surface staining, cells were washed twice with FACS buffer and analyzed directly or fixed for downstream intracellular staining and/or analysis the next day. Cell fixation was achieved using the Foxp3 Transcription Factor Fixation/Permeabilization buffer (eBioscience) when staining for transcription factors, or the Cytofix/Cytoperm Fixation/Permeabilization buffer (BD Biosciences) when staining for cytokines, following manufacturer's instructions. Brefeldin A (BioLegend) was added to all buffers prior to fixation when staining for cytokines. After fixation, cells were washed twice with FACS buffer, stained for intracellular proteins (antibodies and dilutions specified in Table S5) in FACS buffer overnight at 4°C and then washed twice with FACS buffer prior to flow analysis. To obtain absolute counts of cells, Precision Count Beads (BioLegend) were added to samples following manufacturer's instructions. Flow cytometry sample acquisition was performed on an LSR Fortessa cytometer (BD), and the collected data was analyzed using FlowJo v10.5.3 software (TreeStar). For cell sorting, the surface staining was performed as

described above under sterile conditions, and cells were acquired and sorted into co-culture media (RPMI (GIBCO) containing 10% FBS (Atlanta Biologicals), 1% penicillin/streptomycin (GIBCO), 1X non-essential amino acids (GIBCO) and 1X β -mercaptoethanol (GIBCO)) using a FACS Aria III sorter (BD). For CD8⁺ T cell analysis, cells were pre-gated on live, singlets, CD45⁺, CD3e⁺, CD4⁻, CD8⁺ (and CD45.1⁺ if congenically labeled) markers. For DC analysis and cell sorting, cells were pre-gated on live, singlets, CD45⁺, CD19⁻, CD3e⁻, NK1.1⁻, Ly6C⁻, MHCII⁺, F4/80⁺, CD11c⁺ and ZsG⁺ if appropriate (also autofluorescence⁻ in lungs to exclude autofluorescent CD11c⁺ alveolar macrophages). For Treg cell analysis, cells were pre-gated on live, singlets, CD45⁺, CD3e⁺, CD8⁻, CD4⁺ and FoxP3⁺ markers (and eTreg cells were further defined as CD44⁺ CD62L⁺ Treg cells), and for cell sorting Treg cells were gated as live, singlets, CD45⁺, CD3e⁺, CD8⁻, CD4⁺ and CD25^{high} and an example gating strategy is shown in [Data S1A](#).

SIIN-tetramer staining

To identify SIIN-reactive CD8⁺ T cells, PE-conjugated SIIN tetramer was added during the surface staining step in the flow cytometry methods described above. PE-conjugated SIIN tetramer was assembled in-house using biotinylated peptide-MHC monomer (NIH Tetramer Core Facility) and PE-streptavidin (Invitrogen) following the NIH tetramerization protocol, and titrated to empirically determine the optimal staining concentration.

In vivo mouse treatments

For DT-mediated cell depletion, DT (Sigma-Aldrich) was diluted in PBS (GIBCO) and administered intraperitoneally (*i.p.*) to deplete FoxP3⁺ Treg cells in *FoxP3*^{DTR} mice, *FoxP3*^{DTR}/WT and *FoxP3*^{DTR}/*Ifngr1*^{-/-} BMCs (1 μ g DT/mouse) or XCR1⁺ DC1 in *XCR1*^{DTR} mice, *XCR1*^{DTR}/WT and *XCR1*^{DTR}/*H2-Ab1*^{-/-} BMCs (0.5 μ g DT/mouse) at the indicated timepoints. For *in vivo* treatments, mice were injected with 100 μ g α CD28 antibody *i.p.* (clone 37.51, Bio X Cell), 1.42x10⁻¹¹ mol IL-12 protein fused to murine serum albumin *r.o.* (IL-12-MSA, manufactured in-house) or 200 μ g IFN γ antibody *i.p.* (clone XMG1.2, Bio X Cell) at the indicated timepoints.

IFN γ ELISpot

ELISpot plates (EMD Millipore) were coated overnight at 4°C with α IFN γ capture antibody (BD Biosciences). Plates were washed and blocked with complete media (DMEM (GIBCO) supplemented with 10% FBS (Atlanta Biologicals), 1% penicillin/streptomycin (GIBCO), and 1X non-essential amino acids (GIBCO)) for 2 h at room temperature (RT). Splenocytes were plated in complete media at 10⁶ cells/well in the presence or absence of 160 nM SIINFEKL peptide (Invivogen). As a positive control, splenocytes were plated in complete media containing 100 ng/mL PMA (Sigma-Aldrich) and 1 μ g/mL ionomycin (Sigma-Aldrich). Plates were incubated overnight at 37°C and 5% CO₂, then developed using the mouse IFN γ ELISpot kit (BD Biosciences), following manufacturer's protocol.

Treg cell transcription factor analysis

To accurately compare differences in Treg cell transcription factor expression, lung and flank KP-zSIIN tumors were implanted into Thy1.2⁺ and Thy1.1⁺ mice, respectively, and tdLN from congenically-labeled mice were combined for downstream processing and flow analysis. Relative expression of transcription factor expression were quantified as the ratio of gMFI values for matched Thy1.2⁺ mLN-derived and Thy1.1⁺ iLN-derived fractions of bulk or eTreg cells, as indicated. The experiment was repeated with reversed congenic marker assignments, i.e. using tdLN samples from Thy1.1⁺ lung- and Thy1.2⁺ flank-tumor-bearing mice, to ensure reproducibility, and the data were pooled. The same experimental approach was used to evaluate transcription factor expression in Treg cells from WT and *Batf3*^{-/-} lung tumor-bearing mice.

GENERATION OF BMC MICE

Host mice were irradiated with 500 rad, allowed to recover for 3 h, and subsequently irradiated again with 550 rad. The next day, BM was harvested from the femur and tibia of donor mice, depleted of T cells using CD90.2 microbeads (Miltenyi Biotec), washed twice with PBS and 10⁷ cells were injected *r.o.* into the irradiated host mice. For mixed BM chimeras, 10⁷ total cells of a 50:50 mixture of BM from donor mice was transferred. A period of at least 6 weeks was allowed for engraftment prior to the start of experiments.

Ex vivo T cell priming co-cultures

DC and Treg cells were FACS-sorted from LN as described above (LN from many mice were pooled to reach appropriate cell yield). SIIN-reactive CD8⁺ T cells were isolated from spleens and LN of naive OT-I TCR-transgenic mice using the untouched CD8⁺ T cell isolation kit (Miltenyi Biotec), following manufacturer's instructions. Isolated CD8⁺ OT-I T cells were washed twice with PBS and stained with CTV dye (Life Technologies) following manufacturer's instructions. For DC:OT-I co-cultures, 5x10³ sorted ZsG⁺ or ZsG⁻ DC were cultured with 5x10⁴ dye-labeled CD8⁺ OT-I T cells, respectively (1:10 DC:T cell ratio). For ZsG⁺ DC:OT-I T cell suppression co-cultures, 5x10³ sorted ZsG⁺ DC1 were cultured with 5x10⁴ dye-labeled CD8⁺ OT-I T cells, in the presence or absence of 6.25x10³ sorted Treg cells (1:8 Treg:OT-I ratio), unless indicated otherwise. For Treg:OT-I suppression co-cultures performed without DC1, various numbers of Treg cells were cultured with 5x10⁴ dye-labeled CD8⁺ OT-I T cells (at the indicated Treg:OT-I ratios) on α CD3/ α CD28-coated plates. Antibody-coated plates were coated overnight at 4°C with 0.2 μ g/mL α CD3 (clone 145-2C11, BD Biosciences) and 0.5 μ g/mL α CD28 (clone 37.51, BD Biosciences) in PBS, washed with PBS, then blocked with co-culture media (RPMI (GIBCO) containing 10% FBS (Atlanta Biologicals), 1% penicillin/streptomycin (GIBCO) and 1X β -mercaptoethanol (GIBCO)) for at least 30 min at RT, prior to adding cells. For all ex vivo T cell priming co-cultures, cells were resuspended in co-culture medium,

added to V-bottom tissue culture-treated 96-well plates and cultured at 37°C and 5% CO₂ for 3 days. Following co-culture, cells were stained and analyzed by flow cytometry. Frequency of proliferated T cells was quantified as the percentage of cells that had undergone one or more rounds of division, gated using an unstimulated, CTV-labeled sample as the undivided reference control. The T cell proliferation index was quantified as the total number of divisions divided by the the number of cells that went into division using the proliferation modeling function in FlowJo v10.5.3 software (TreeStar). Expression of T cell activation markers was also assessed by flow staining as described. For co-culture experiments performed in the presence of additional biomolecules, 5 µg/mL αCD28 (clone 37.51, BD Biosciences), 10 nM IL-12 (using IL-12-MSA fusion protein generated in-house) or 10 µg/mL αMHCII (clone M5/114, Bio X Cell) were added at the beginning of co-culture where indicated.

Generation of BM-DC

BM-DC generation protocol was adapted from de Mingo Pulido et al.¹²⁵ BM was harvested from the femur and tibia of *p40-IRES-eYFP* mice, passed through a 70 µm filter, ACK-lysed and cultured at a density of 2x10⁶ cells/ml in RPMI (GIBCO) supplemented with 10% FBS (Atlanta Biologicals), 1% penicillin/streptomycin (GIBCO), 25 mM HEPES (GIBCO), 1X non-essential amino acids (GIBCO), 10 mM sodium pyruvate (GIBCO), 1X β-mercaptoethanol (GIBCO), 100 ng/mL recombinant human FLT3-L (Bio X Cell), and 5 ng/mL recombinant mouse GM-CSF (BioLegend) for 6 days at 37°C and 5% CO₂. On day 6, floating and semi-adherent cells were collected as BM-DC, frozen in 10% DMSO (Sigma-Aldrich) in FBS (Atlanta Biologicals) and stored in liquid nitrogen.

BM-DC:Treg cell co-cultures

Treg cells were FACS-sorted from LN as described above. Frozen *p40-IRES-eYFP* BM-DC were thawed and cultured in RPMI (GIBCO) supplemented with 10% FBS (Atlanta Biologicals), 1% penicillin/streptomycin (GIBCO), 25 mM HEPES (GIBCO), 1X non-essential amino acids (GIBCO), 10 mM sodium pyruvate (GIBCO), 1X β-mercaptoethanol (GIBCO), 100 ng/mL recombinant human FLT3-L (Bio X Cell), and 5 ng/ml recombinant mouse GM-CSF (BioLegend) for 2 days at 37°C and 5% CO₂. BM-DC were then washed in PBS and cultured overnight in 1 µg/mL Poly(I:C) (Invivogen) in co-culture media (RPMI (GIBCO) containing 10% FBS (Atlanta Biologicals), 1% penicillin/streptomycin (GIBCO) and 1X β-mercaptoethanol (GIBCO)) at 37°C and 5% CO₂ to generate mature BM-DC. On the next day mature BM-DC were collected and washed twice with PBS, prior to addition to assays. For BM-DC:Treg cell co-cultures, 2x10⁴ mature BM-DC and 2.5x10⁴ sorted Treg cells were resuspended in co-culture medium with 10 nM IL-2 (using IL-2-MSA fusion protein generated in-house), added to V-bottom tissue culture-treated 96-well plates and cultured at 37°C and 5% CO₂ for 24 h. Following co-culture, cells were stained and analyzed by flow cytometry. A representative gating strategy of BM-DC1 is shown in [Data S1B](#).

Tissue section preparation and immunostaining

Adapted from Gerner et al.¹²⁶ LN were harvested, fixed in periodate-lysine-parafomaldehyde buffer (0.05 M phosphate buffer containing 0.1 M lysine, 2 mg/mL NaIO4, and 1% of paraformaldehyde (Electron Microscopy Grade), pH 7.4) overnight at 4°C, followed by cryoprotection in 30% sucrose in PBS for 24 h at 4°C. LN were then carefully cleaned of fat, embedded in 100% OCT in cryomolds, snap-frozen by floating the cryomolds on a solution of 2-methylbutane cooled by dry ice and stored at -80°C until processing. Frozen LN were completely sectioned (10 µm thickness) using Cryostar NX70 (Thermo Scientific) to make sure that imaged tissue cross-sections contained all representative LN regions. Tissue sections were left to dry for 30 min at RT, post-fixed in ice-cold acetone for 10 min at -20°C, then left to dry again for 30 min at RT and stored at -20°C. For immunostaining, sections were first warmed to RT, washed twice with PBS and incubated with blocking buffer (PBS containing 1% BSA, 1% normal mouse serum, 10% normal goat serum, and 0.3% Triton X-100) for 2 h at RT. Tissue sections were then stained with primary antibody (chicken polyclonal αGFP, 1:1000; abcam) diluted in blocking buffer for 2 h at RT, washed three times with wash buffer (PBS with 0.3% Triton X-100), followed by staining with secondary antibody (goat anti-chicken AF488 1:500, Jackson ImmunoResearch) diluted in blocking buffer for 1 h at RT. Next, samples were washed three times with wash buffer and stained with fluorophore-conjugated antibodies (FoxP3-AF750 clone 1054C, 1:100, R&D Systems; CD45.1-APC clone A20, 1:100, Biolegend) diluted in blocking buffer for 1 h at RT. Then, nuclei were counterstained with 1.5 µm propidium iodide (1:1000, Sigma-Aldrich) diluted in wash buffer for 10 min at RT, followed by a wash in PBS. Samples were mounted using Pro-Long Diamond Antifade Mountant (Thermo Fisher Scientific).

Imaging

Tissue sections were imaged using the TissueFAXS Plus automated slide scanning system (TissueGnostics, USA) combining a Zeiss Axio Imager 2 upright microscope with a Märzhäuser motorized stage (Märzhäuser Wetzlar). We utilized the Zeiss 20x Plan-Neofluor 0.5 N.A. air objective, in combination with filters sets (from Chroma Technology, USA) with the following specifications: AF488 (470/24) ET470/30x T495lpxr ET515/30m, AF750 (740/20) ET740/40x T770lpxr ET780lp, multiband dichroic qTexasRed/qCy5 (550/15, 640/30). A Lumencor Spectra 3 LED light engine (500 mW per channel) provided excitation. Fluorescence images were captured using a Hamamatsu Orca Flash 4.0 V2 cooled digital CMOS camera C11440-22CU. Exposure times were 94 ms for AF488, 146 ms for AF750, 10 ms for qTexasRed and 48 ms for qCy5 channels. Tissue sections were acquired as z-stacks in a process called extended focus, with a 3 µm step size, including one step above and one step below the focal plane. Extended focus takes each in-focus area of each image within the z stack and combines those regions into a single image. Image processing included stitching performed using the TissueFAXS capture/control software.

Image processing and spatial analysis

Images were exported as single channel TIFF files using the TissueFAXS Viewer software (TissueGnostics USA) and downstream image analysis was completed in Imaris software v9.7.2 (Bitplane) and using custom scripts in Python. Imaris Surface objects were created for FoxP3⁺ Treg cells (smoothing sigma = 0.5 μ m, intensity threshold = 17.2, seed point diameter = 3.00 μ m, seed point quality filter = 1.0), XCR1⁺ DC1 (smoothing sigma = 0.20 μ m, background subtraction rolling ball radius = 5.00 μ m, background subtraction threshold = 8.69, seed point diameter = 5.00 μ m, seed point quality threshold = 2.07, size threshold \geq 50.0 voxels), CD45.1⁺ CD8⁺ OT-I T cells (smoothing sigma = 0.5 μ m, intensity threshold = 16.7, seed point diameter = 6.00 μ m, seed point quality threshold = 4.87, area threshold \geq 11.5 μ m²) and CD45.1⁺ CD8⁺ OT-I T cell clusters (smoothing sigma = 0.5 μ m, intensity threshold = 9.12, area threshold $>300\mu$ m²). Surfaces for FoxP3⁺ Treg cells, XCR1⁺ DC1 cells and CD45.1⁺ CD8⁺ OT-I T cells were further segmented using the “Split touching objects” function. A surface was also made for the entire lymph node using the nuclear channel (smoothing sigma = 5.00 μ m, intensity threshold = 10.0). For each surface set, the surface area and centroid coordinates were exported and collated across images. For each CD8⁺ OT-I T cell cluster surface, the area of the cluster was used to calculate the radius. The microniche area for each CD8⁺ OT-I T cell cluster was defined using the radius of the CD8⁺ OT-I T cell cluster plus 5 μ m, 10 μ m, 15 μ m and 20 μ m. Distance matrices encoding the distance between the centroid of the CD8⁺ OT-I T cell cluster and centroids all DC1 and Treg cells in the image were generated. These distance matrices were thresholded using the microniche radius to find the DC1 and Treg cells that were positioned within each microniche. Finally, a new distance matrix was calculated between the DC1 and Treg cells within each microniche to find the minimum distance from each Treg cell to a DC1. Code made available: <https://github.com/awedwards/DC-Treg-CD8T-interactions-project>. Example images of the segmentation and the microniche analysis workflow are provided in Data S1C–F.

Generation of IL-2 and IL-12 fusion proteins

Extended half-life cytokine-MSA fusions were generated as previously described.^{127,128} HEK293 cells (at 1 million cells/ml) were transfected with sterile-filtered plasmid DNA (1 mg/L cell culture) using polyethylenimine (2 mg per liter cell culture) in OptiPro serum-free medium (40 mL/L cell culture) (Thermo Fisher). His-tagged proteins were isolated from HEK293 supernatant using TALON Metal Affinity Resin (Takara Bio Inc.). Cytokine-fusion proteins were then further purified by size exclusion chromatography using a HiLoad 16/600 Superdex 200 pg column on an ÄKTA FPLC system (GE Healthcare) that had been pretreated for 4 h with 1 M NaOH to remove endotoxin and subsequently equilibrated in sterile PBS (Corning). After purification, all proteins were buffer exchanged into sterile PBS (Corning), 0.2 micron sterile-filtered (Pall Corporation), and confirmed to contain minimal endotoxin (<0.1 EU per injection) using a chromogenic LAL assay (Lonza). To confirm their molecular weights, proteins were run alongside a Novex Prestaind Sharp Protein Ladder on a 4–12% NuPAGE Bis-Tris protein gel (Life Technologies) with 1% MES running buffer. Proteins were flash-frozen and stored at –80°C, but before therapeutic injection, cytokine fusion proteins were warmed to room temperature.

Cytokine measurements in LN supernatant

LN were homogenized in T-PER Tissue Protein Extraction Reagent (Thermo Fisher Scientific) supplemented with cOmplete™ Protease Inhibitor Cocktail (Sigma-Aldrich) and centrifuged for 5 min at 500 g. LN supernatant was collected, flash-frozen and stored at –80°C. IFN γ and IL-2 cytokines were quantified via ELISA (Mouse IFN γ DuoSet ELISA, R&D Systems; Mouse IL-2 DuoSet ELISA) following manufacturer’s instructions.

Seq-Well scRNA-seq

For scRNA-seq of ex vivo-primed T cells, CD8⁺ OT-I T cells and ZsG⁺ DC1 sorted from tumor-draining mLN were cultured alone or in the presence of Treg cells sorted from tumor-draining mLN (added at the 1:8 Treg:OT-I ratio) as described above. After the 3-day co-culture, cells were collected for sequencing. For scRNA-seq of Treg cells, LN were mashed through a 70 μ m filter into RPMI (GIBCO), then incubated with α CD16/CD32 (clone 93, BioLegend) in FACS buffer (PBS (GIBCO) with 1% FBS (Atlanta Biologicals) and 2 mM EDTA (Invitrogen)) for 15 min at 4°C, washed with FACS buffer and stained with a mix of α CD45-APC (1:200, clone 30-F11, Biolegend) and Total-seq A mouse hashtag antibody (1:100, clone 30-F11, Biolegend) in FACS buffer to label individual mice (hashtag labeling was only performed for tdLN, not naive LN). Cells were then washed twice in FACS buffer and tdLN cells from multiple mice were pooled together for subsequent CD4⁺ T cell enrichment sing the mouse CD4⁺ T cell isolation kit (Miltenyi Biotec), following manufacturer’s instructions. Next, cells were stained for FACS and Treg cells were sorted as previously described. Cells from ex vivo co-cultures and sorted Treg cells were processed for scRNA-seq using the Seq-Well platform with second strand chemistry, as previously described.^{129,130} Whole transcriptome libraries were barcoded and amplified using the Nextera XT kit (Illumina) and were sequenced on a Novaseq 6000 (Illumina). Hashtag oligo libraries were amplified as described previously and were sequenced on a Nextseq 550.¹³¹

Processing of cell hashing data

Cell hashing data was aligned to HTO barcodes using CITE-seq-Count v1.4.2.¹³² To establish thresholds for positivity for each HTO barcode, we first performed centered log-ratio normalization of the HTO matrix and then performed k-medoids clustering with k = 5 (one for each HTO). This produced consistently five clusters, each dominated by one of the 5 barcodes. For each cluster, we first identified the HTO barcode that was dominant in that cluster. We then considered the threshold to be the lowest value for that HTO barcode among the cells classified in that cluster. To account for the scenario in which this value was substantially lower

than the rest of the values in the cluster, we used Grubbs' test to determine whether this threshold was statistically an outlier relative to the rest of the cluster. If the lower bound was determined to be an outlier at $p = 0.05$, it was removed from the cluster, and the next lowest value was used as the new threshold. This procedure was iteratively applied until the lowest value in the cluster was no longer considered an outlier at $p = 0.05$. Cells were then determined to be "positive" or "negative" for each HTO barcode based on these thresholds. Cells that were positive for multiple HTOs or were negative for all HTOs were excluded from downstream analysis. To account for differences in sequencing depth between samples, these steps were performed separately for each Seq-Well array that was processed.

scRNA-seq data processing and visualization

Raw read processing of scRNA-seq reads was performed as previously described.¹³³ Briefly, reads were aligned to the mm10 reference genome and collapsed by cell barcode and unique molecular identifier (UMI). Then, cells with less than 1000 (for the co-culture dataset) or 700 (for the Treg cell dataset) unique genes detected and genes detected in fewer than 5 cells were filtered out, and the data for each cell was log-normalized to account for library size. Genes with log-mean expression values greater than 0.1 and a dispersion of greater than 1 were selected as variable genes, and the ScaleData function in Seurat v2.3.4¹³⁴ was used to regress out the number of UMI and percentage of mitochondrial genes in each cell. Principal components analysis was performed. The number of principal components used for visualization was determined by examination of the elbow plot, and two-dimensional embeddings were generated using uniform manifold approximation and projection (tSNE). Clusters were determined using Louvain clustering, as implemented in the FindClusters function in Seurat. In the *ex vivo* co-culture dataset, CD8⁺ T cells were specifically identified based on the expression of canonical CD8⁺ T cell transcripts including *CD3e*, *CD8a*, *Lck* and *Thy1*, and these CD8⁺ T cell clusters were selected for further analysis. The CD8⁺ T cells were reprocessed with the same processing and clustering steps described above. DEG analysis was performed for the CD8⁺ T cells between the two co-culture conditions using the FindMarkers function. Gene signature scores defined as the top 50 DEGs of the *in vivo*-primed CD8⁺ T cells from tumor-draining mLN and iLN²⁴ were calculated using Seurat's AddModuleScore function¹³⁵ and compared between the two co-culture conditions. In the Treg cell dataset, Treg cells were identified based on the expression of canonical Treg cell transcripts including *CD3e*, *CD4*, *FoxP3* and *Il2ra*, and the contaminating cell clusters were removed. Naive T cell gene set signature scores^{69–71} were obtained from MSigDB¹³⁶ and calculated using Seurat's AddModuleScore function¹³⁵ and compared across Treg cell clusters. Clusters that contained activated Treg cells were selected for further analysis. These cells were reprocessed with the same processing and clustering steps described above. DEG analysis was performed for each cluster and between indicated cell populations using the FindMarkers function.

Paired single-cell TCR-seq and analysis

Paired TCR-seq and read alignment was performed as previously described.¹³⁷ Briefly, whole transcriptome amplification product from each single-cell library was enriched for TCR transcripts using biotinylated *Tcrb* and *Tcra* probes and magnetic streptavidin beads. The enrichment product was further amplified using V-region primers and Nextera sequencing handles, and the resulting libraries were sequenced on an Illumina Novaseq 6000. Processing of reads was performed using the Immcantation software suite.^{138,139} Briefly, reads were aggregated by cell barcode and UMI, and UMI with under 10 reads were discarded. ClusterSets.py was used to divide sequences for each UMI into sets of similar sequences. Only sets of sequences that comprised greater than 90% of the sequences obtained for that UMI were considered further. Consensus sequences for each UMI were determined using the BuildConsensus.py function. Consensus sequences were then mapped against TCRV and TCRJ IMGT references sequences with IgBlast. Sequences for which a CDR3 sequence could not be unambiguously determined were discarded. UMI for consensus sequences were corrected using a directional UMI collapse, as implemented in UMI-tools.¹⁴⁰ TCR sequences were then mapped to single cell transcriptomes by matching cell barcodes. If multiple *Tcra* or *Tcrb* sequences were detected for a single cell barcode, then the corresponding sequence with the highest number of UMI and raw reads was retained. Expanded clones were defined as multiple cells from the same mouse (i.e. with same hashtag signal where hashing antibodies were used) containing identical CDR3β junction nucleotide sequences. Clonal size was defined as the number of cells from a given mouse (identified based on the hashtag signal where hashing antibodies were used) that share the same CDR3β junction nucleotide sequence.

Re-analysis of dataset from Sade-Feldman et al. (Cell 2018)

Patient characteristics and scRNA-seq of tumor-infiltrating immune cells from metastatic melanoma patients published by Sade-Feldman et al.⁹³ were downloaded from the Gene Expression Omnibus (GEO, accession GSE120575). This dataset was processed as previously described.¹⁴¹ Briefly, a Seurat v3.0.0¹³⁴ object was created such that the counts slot and data slot were populated with TPM counts and log(TPM+1) counts, respectively. Highly variable genes were identified (FindVariableFeatures) and the data was scaled (ScaleData, while regressing out percentage mitochondrial content per cell and the number of detected reads per cell) followed by dimensionality reduction with PCA using Seurat's standard preprocessing procedure. Clusters were determined using FindNeighbors and FindClusters Seurat functions with 21 principal components (clustering resolution 0.6). Subsequently, hallmark IFN response gene set signature scores^{136,142} for cells within the FoxP3⁺ Treg cell cluster were calculated using Seurat's AddModuleScore function¹³⁵ and compared between ICB-responders and non-responders.

QUANTIFICATION AND STATISTICAL ANALYSIS

Statistical analyses were performed using GraphPad Prism (GraphPad) and R. All data are shown as mean \pm SEM, unless otherwise indicated. For flow cytometry and immunofluorescence data, statistical analyses were performed with Mann-Whitney U (MWU) test for comparison of two groups, Kruskal-Wallis (KW) test for comparison of more than two groups, or two-way ANOVA for multiple comparisons with * $p < 0.05$; ** $p < 0.01$; *** $p < 0.001$; **** $p < 0.0001$; ns = not significant. Nonparametric tests were used as the small sample sizes in our study did not allow us to assume a normal distribution.¹⁴³ For scRNA-seq differential gene expression and pathway analyses, p values were calculated using a two-sided MWU test and adjusted with Bonferroni correction.